Journal of Fluids and Structures 123 (2023) 104004

Contents lists available at ScienceDirect

Journal of Fluids and Structures

journal homepage: www.elsevier.com/locate/jfs

Wake-induced vibration and heat transfer characteristics of three tandem semi-circular cylinders

Junlei Wang [a], Ye Zhang [a], Guobiao Hu [b,*], Wenming Zhang [c,*]

[a] School of Mechanical and Power Engineering, Zhengzhou University, Zhengzhou 450000, China
[b] Internet of Things Thrust, The Hong Kong University of Science and Technology (Guangzhou), Nansha, Guangzhou, Guangdong 511400, China
[c] State Key Laboratory of Mechanical System and Vibration, School of Mechanical Engineering, Shanghai Jiao Tong University, 800 Dongchuan Road, Shanghai 200240, China

ARTICLE INFO

Keywords:
Wake-induced vibration
Aerodynamic response
Nusselt number
Heat transfer
Temperature distribution

ABSTRACT

This paper studies the wake-induced vibration (WIV) and heat convection of the downstream tandem bluff bodies under the influence of an upstream bluff body at $Re = 200$ and $Pr = 0.7$. For the reduced fluidic velocity (U_r) in the range of 1–16 and different bluff body diameter ratios (d/D), three wake interference patterns, namely, the quasi-co-shedding (QCS) pattern, the co-shedding (CS) pattern, and the coupling between QCS and CS (QCS-CS) are formed due to the interference between the shear layer and vortex shedding process. The occurrence conditions of the three patterns are closely related to U_r and d/D. The vibration response of the midstream bluff body is roughly consistent with that of a heat-isolated semi-circular cylinder (HISC) if d/D is small. By increasing d/D, the vibration amplitude of the midstream bluff body first increases, then decreases with U_r. The vibration amplitude of the downstream bluff body starts to increase from small d/D and then can maintain a high value with the increase of U_r, even at large d/D. Compared with the HISC, the tandem configurations can help reduce the drag force. Because of the wake interference and the 'blocking effect' from the upstream bluff body, although the heat convection of the midstream and downstream bluff bodies can be effectively strengthened through WIV, the time-averaged Nusselt numbers (Nu_A) of the midstream and downstream bluff bodies are still lower than that of the HISC. Besides, heat transfer efficiency has been found to correlate with the transverse vibration amplitude of bluff bodies. Moreover, it is revealed that there is a trade-off between the heat transfer efficiency of the equipment and its service lifespan because increasing the vibration amplitude enhances convection but also increases the risk of potential damage to the structural integrity.

1. Introduction

Understanding fluid flow characteristics around bluff structures and conducting flow-induced vibration (FIV) analyses are of significant importance for the structural health monitoring and maintenance of many practical infrastructures, such as nuclear reactors (Huang et al., 2008), gas pipelines (Zhu et al., 2022), and evaporators (Peng et al., 2022). Heat exchangers are indispensable components of the above infrastructures, and tube heat exchangers are pretty typical in the industry. When the fluid flows through a bluff body, vortices shed off alternatively behind the bluff body after Reynolds number (Re) exceeds 40 (Païdoussis et al., 2011); a

---

* Corresponding authors.
E-mail addresses: guobiaohu@hkust-gz.edu.cn (G. Hu), wenmingz@sjtu.edu.cn (W. Zhang).

https://doi.org/10.1016/j.jfluidstructs.2023.104004
Received 11 May 2023; Received in revised form 1 October 2023; Accepted 9 October 2023

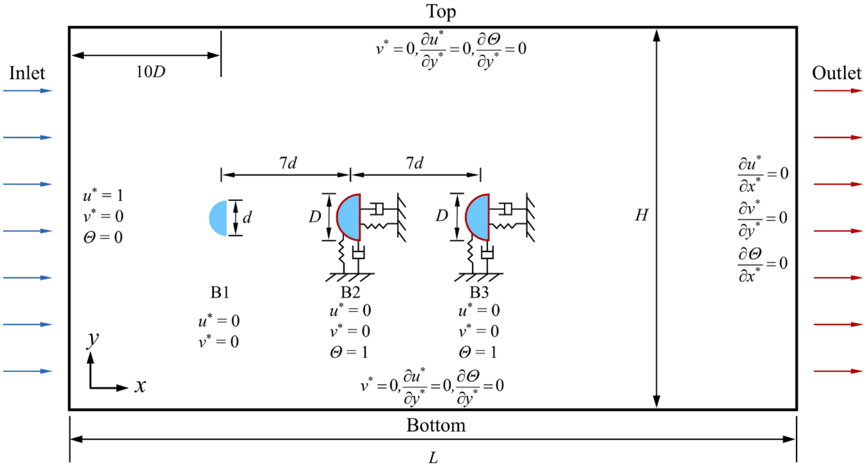

Fig. 1. Schematic of the computational domain and the implementation of the boundary conditions (not in real scale).

periodically fluctuating force is exerted on the bluff body, causing it to vibrate; the vibration of the bluff body generates a feedback effect on vortices leads to a transformation of vortices and force. The above-described fluid-structure interaction process is the so-called flow-induced vibration (FIV) phenomenon (Xu et al., 2019; Wang et al., 2020; Khan et al., 2022; Ding et al., 2018).

Over the past decades, heat exchangers were usually designed bulky to prolong their service lifespans. Lots of efforts have been devoted to enhancing heat transfer using fixed bluff bodies. For example, Ambreen *et al.* (Ambreen and Kim, 2018) studied the influences of modified corners on the fluid flow around and heat transfer characteristics of a cuboid bluff body. Their study showed that appropriately modifying the corners could reduce the pressure resistance and increase the heat transfer coefficient. Chhabra *et al.* (Dhiman et al., 2005) investigated the effects of different boundary conditions on the heat transfer rate of a cuboid bluff body. They also developed heat transfer correlations of a cuboid bluff body at constant heat flux and stable temperature conditions. Zafar *et al.* (Zafar and Alam, 2019) numerically investigated the influence of the corner radius on the heat transfer of a cuboid bluff body. The results revealed that with the increase of the corner radius, the heat transfer efficiency increased by up to 33.0%.

In recent years, due to the severe environmental pollution problem and the energy crisis, there has been an impending demand for developing low-cost and eco-friendly equipment. One representative measure is the design of small-sized lightweight heat transfer exchangers. Unfortunately, the occurrence probability of the FIV phenomenon in these heat transfer exchangers is increasing (Goyder, 2002; Ali et al., 2021). Therefore, FIV analysis has become a pivotal criterion (Pettigrew and Taylor, 2003a, 2003b) in designing and manufacturing heat exchangers over the past years. Generally speaking, for the running heat exchangers, the essence of FIV is the process in which the energy input from the fluid continuously accumulates and dissipates on heat transfer tubes. Once the heat exchangers are in operation, the fluid in the heat exchangers will accumulate energy on the heat transfer tubes due to viscosity. It is difficult and even impossible to prevent the FIV of heat exchanger tubes (Wambsganss, 1981). FIV does not require additional energy expenditure. Thus, many researchers proposed utilizing fluids to induce the vibration of heat transfer tubes to improve heat transfer efficiency. Go *et al.* (Go, 2003) proposed a novel micro fin array heat sink that used FIV to improve heat transfer. The heat transfer efficiency increased by 11.5% compared with a plane-wall heat sink at an air velocity of 5.5 m/s. Ding *et al.* (Ding et al., 2022) investigated the effect of an upstream stationary cylinder on heat transfer characteristics and FIV of the downstream elastically supported cylinder. The averaged Nusselt number of the downstream cylinder increased by up to 150.42% when the gap between the two cylinders was set large enough. Duan *et al.* (Duan et al., 2017) found that the vibration of the heat tube within the sub-millimeter level could increase the average Nusselt number of a heat exchanger by 6.5%. Cheng *et al.* (Cheng et al., 2009) proposed a new approach to enhance the heat transfer of a tube bundle by using FIV. The outside convective heat transfer coefficient increased by more than two times, and the fouling resistance decreased by 66% compared with a fixed tube bundle.

Many researchers have conducted experimental studies and numerical simulations of fluid flow and heat transfer experiments in circular and square bluff bodies. In recent years, research on fluid flow and heat transfer problems of semi-circular bluff bodies have gradually emerged. Nada *et al.* (Nada et al., 2006) conducted experimental and numerical studies on fluid flow and heat transfer characteristics around semi-circular tubes. They found that the arrangement of curved surfaces facing the flow leads to a higher Nusselt number than that of flat surfaces facing the flow. Parthasarathy *et al.* (Parthasarathy et al., 2017) studied the flow and heat transfer characteristics of a row of semi-circular cylinders under different gap ratios at $Re = 100$ and discussed the streamline and isotherm contours for various gap ratios. Kumar *et al.* (Kumar et al., 2020) enhanced convective heat transfer using D-shaped semi-circular bluff bodies in a laminar channel flow. Compared to the ordinary cylinder, the FIV of the D-shaped semi-circular bluff body improved heat transfer efficiency by more than 30%. Besides, semi-circular cylinders could offer space economy in the specific heat transfer area. At the same time, semi-circular cylinders have some similar characteristics to cuboid bluff bodies due to the existence of edges and corners, which might be beneficial for designing innovative energy harvesters and developing new techonologies (Barrero-Gil et al., 2022; Zhang et al., 2021; KOIDE et al., 2002; Zhang et al., 2022). Analogous to a circular cylinder, fluid flow and heat transfer around a semi-circular cylinder have a variety of engineering applications, such as novel type heat exchangers (Mahendra and Kumar, 2023) and thermal cooling (Verma and De, 2022). The tandem arrangement is a popular configuration in multi-bluff body devices. However, there is limited literature on studying the FIV and heat transfer characteristics of tandem semi-circular bluff bodies.

Inspired by previous studies, the wake-induced vibration (WIV) and heat transfer characteristics of three tandem semi-circular cylinders with different-diameter upstream semi-circular cylinders at $Re = 200$ and $Pr = 0.7$ are numerically investigated in this work. The influences of reduced velocity and different diameters on the wake interference model, WIV trajectory response, temperature distribution, and Nusselt number are discussed. Finally, a series of suitable operating conditions are determined. Under these conditions, the amplitudes of the bluff bodies are moderate, and the Nu_A of the midstream and downstream bluff bodies has significantly improved.

2. Computational domain and boundary conditions

Fig. 1 shows the computational domain with a size of $L \times H$, where D is the diameter of the midstream and downstream bluff bodies. The left and right sides of the computational domain are set as the inlet and outlet, respectively. The upstream bluff body (B1) with a diameter of d is located at a distance of $10D$ from the inlet boundary. The streamwise spacing between B1 and the midstream bluff body (B2) is $7d$, the same as the distance between B2 and the downstream bluff body (B3). In the present work, the diameter of B1, i.e., d, will vary and take the values of $0.7D$, $0.8D$, $1.0D$, $1.2D$, and $1.4D$. The Reynolds number (Re) and the Prandtl number (Pr) are fixed at 200 and 0.7, respectively.

The dimensionless boundary conditions are also illustrated in Fig. 1. The inlet boundary condition is set as a uniform flow with a constant temperature, i.e., $u^* = 1$, $v^* = 0$, $\Theta = 0$, where u^* and v^* are the x- and y-directional components, and Θ is the temperature variable, defined as $\Theta = (T - T_\infty)/(T_w - T_\infty)$, where T_∞ is the freestream fluid temperature, and T_w is the surface temperature of B2 and B3, T is the field temperature in the computation domain. Symmetric boundary conditions are applied on the two lateral sides. The tangential velocities, the normal velocity gradient, and the temperature gradient are zero, i.e., $v^* = 0$, $\frac{\partial u^*}{\partial y^*} = 0$, $\frac{\partial \Theta}{\partial y^*} = 0$. The Neumann boundary condition is applied on the outlet boundary: $\frac{\partial u^*}{\partial x^*} = 0$, $\frac{\partial v^*}{\partial x^*} = 0$, $\frac{\partial \Theta}{\partial x^*} = 0$. The non-slip boundary condition is applied on the three bluff body surfaces: $u^* = 0$, $v^* = 0$, and the constant wall temperature is applied on the B2 and B3, i.e., $\Theta = 1$.

The dimensionless variables are defined as:

$$u^* = \frac{u}{U_\infty}, x^* = \frac{x}{D}, v^* = \frac{v}{U_\infty}, y^* = \frac{y}{D}, t^* = \frac{tU_\infty}{D}, p^* = \frac{p}{\rho U_\infty^2}$$

where u and v are the x-and y-directional velocity components in the Cartesian coordinate system, U_∞ is the freestream fluid velocity, t is the time, ρ is the fluid density, p is the pressure, $Re = \rho U_\infty D/\mu$, and $Pr = \mu c_p/\lambda$, where μ is the dynamic viscosity, c_p is the specific heat, and λ is the thermal conductivity.

3. Numerical approach

3.1. Governing equations and integration scheme

Under the subcritical Re, the forced convection dominates heat transfer in limited environments. The heat transfer effect caused by natural convection can be neglected because the air composition is nearly constant, and the thermal physical properties do not change significantly with temperature.

Hence, constant thermal physical properties are adopted in this study, the buoyancy of fluid and the natural convective heat transfer are neglected, and the forced convective heat transfer is considered. The dimensionless governing equations for 2D viscous incompressible flow can be written as:

The mass conservation equation:

$$\frac{\partial u^*}{\partial x^*} + \frac{\partial v^*}{\partial y^*} = 0 \tag{1}$$

The momentum conservation equation:

$$\frac{\partial u^*}{\partial t^*} + \frac{\partial (u^* u^*)}{\partial x^*} + \frac{\partial (u^* v^*)}{\partial y^*} = -\frac{\partial p^*}{\partial x^*} + \frac{1}{Re}\left(\frac{\partial^2 u^*}{\partial x^{*2}} + \frac{\partial^2 u^*}{\partial y^{*2}}\right) \tag{2}$$

$$\frac{\partial v^*}{\partial t^*} + \frac{\partial (u^* v^*)}{\partial x^*} + \frac{\partial (v^* v^*)}{\partial y^*} = -\frac{\partial p^*}{\partial y^*} + \frac{1}{Re}\left(\frac{\partial^2 v^*}{\partial x^{*2}} + \frac{\partial^2 v^*}{\partial y^{*2}}\right) \tag{3}$$

The energy conservation equation:

$$\frac{\partial \Theta}{\partial t^*} + \frac{\partial (u^* \Theta)}{\partial x^*} + \frac{\partial (v^* \Theta)}{\partial y^*} = \frac{1}{Re \cdot Pr}\left(\frac{\partial^2 \Theta}{\partial x^{*2}} + \frac{\partial^2 \Theta}{\partial y^{*2}}\right) \tag{4}$$

For 2D low subcritical flow, except Eq. (2) - (4), the governing equation shows the turbulence viscosity. The built-in Wall-Adapting Local Eddy (WALE) model is employed in the simulation for its excellent performance in addressing wall-involved laminar and turbulent simulation problems (Qi et al., 2022; Dai et al., 2022; Doerksen et al., 2022), and the viscosity coefficient in the WALE model can be written as:

$$\upsilon_t = \Delta^2 \frac{\left(G^d_{\alpha\beta} G^d_{\alpha\beta}\right)^{3/2}}{\left(S_{\alpha\beta} S_{\alpha\beta}\right)^{5/2} + \left(G^d_{\alpha\beta} G^d_{\alpha\beta}\right)^{5/4}} \tag{5}$$

$$\begin{cases} S_{\alpha\beta} = \dfrac{1}{2}\left(\dfrac{\partial u^*}{\partial y^*} + \dfrac{\partial v^*}{\partial x^*}\right) \\ G^d_{\alpha\beta} = \dfrac{1}{2}\left(g^2_{\alpha\beta} + g^2_{\beta\alpha}\right) - \dfrac{1}{3}\delta_{\alpha\beta} g^2_{\gamma\gamma} \\ g_{\alpha\beta} = \dfrac{\partial u^*}{\partial y^*} \\ \Delta = C_w (\mathrm{Vol})^{1/3} \end{cases} \tag{6}$$

where Δ is the filter scale, C_w is the WALE constant, $S_{\alpha\beta}$ is the strain rate tensor, Vol is the local lattice size, δ is the Kronecker delta.

The local Nusselt number Nu_L on the bluff body surface is defined as:

$$Nu_L = \frac{hD}{\lambda} \tag{7}$$

where h is the local heat transfer coefficient. The surface-averaged Nusselt number Nu_S is calculated by averaging the Nu_L over the surface of the bluff body:

$$Nu_S = \frac{1}{2\pi} \int_0^{2\pi} Nu_L d\varphi \tag{8}$$

where φ is the central angle of the bluff body, the time-averaged Nusselt number Nu_A is obtained by integrating Nu_S over one vibration period:

$$Nu_A = \frac{1}{T^*} \int_0^{T^*} Nu_S dt^* \tag{9}$$

where T^* is the time period of the bluff body oscillation.

Bluff bodies B2 and B3 can conduct x- and y-directional vibrations, indicating that they have two degrees of freedom. The mass-spring-damping equation is used to describe the oscillations of B2 and B3:

$$\ddot{X} + \frac{4\zeta\pi}{U_r}\dot{X} + \frac{4\pi^2}{U_r^2} X = \frac{4C_D}{\pi m^*} \tag{10}$$

$$\ddot{Y} + \frac{4\zeta\pi}{U_r}\dot{Y} + \frac{4\pi^2}{U_r^2} Y = \frac{4C_L}{\pi m^*} \tag{11}$$

where $\ddot{X}$, $\dot{X}$, X are the dimensionless acceleration, velocity, and displacement, respectively, in the x-direction. $\ddot{Y}$, $\dot{Y}$, Y are the corresponding variables in the y-direction. X and Y represent the ratio of the actual displacement to the diameter of the bluff body. $\zeta = \frac{C}{2\sqrt{mK}}$ is the damping ratio. K is the spring stiffness, and m is the mass of the bluff body. $U_r = \frac{U_\infty}{f_n D}$ is the reduced velocity, where $f_n = \frac{1}{2\pi}\sqrt{\frac{K}{m}}$ is the natural frequency of the structure. In this study, the frequency is nondimensionalized with the factor D/U_∞, to give the dimensionless frequency. $C_D = \frac{2F_D}{\rho U_\infty^2 D}$ is the drag force coefficient, $C_L = \frac{2F_L}{\rho U_\infty^2 D}$ is the lift force coefficient, F_D and F_L represent the drag and lift forces, respectively. For the semi-circular cylinder $m^* = \frac{8m}{\rho L_b D^2 \pi}$ is the mass ratio and defined as 2.0 in the present study. L_b is the length of the bluff body, in 2D numerical simulations, L_b has a default value of 1 m. Moreover, in the present study, the dimensionless transverse vibration amplitude can be defined as:

$$Y^{max} = \sqrt{\frac{2}{N} \sum_{i=1}^{N} \left(Y_i - Y^{mean}\right)^2} \tag{12}$$

where N is the number of the values in the time series for statistics, and i starts from a relatively stable vibration period, Y^{mean} is the mean transverse displacement.

The traditional CFD solvers are generally mesh-based solutions, implying the need to go through a lengthy meshing process. For every CFD study, a large amount of time will be dedicated to the meshing, which represents a fatal drawback for users. In recent years, alternative particle-based methods have been emerging to overcome these drawbacks. The commercial software XFlow based on the

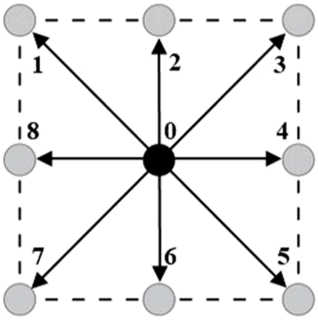

Fig. 2. D2Q9 discrete velocity model.

Lattice Boltzmann Method (LBM) provides new alternatives to solve complex fluid-thermal-structure interactions. The Boltzmann transport equation (BTE) in the LBM derived from statistical physics is very suitable for calculating the transient aerodynamics of complex geometry in CFD. The standard BTE with a single relaxation time can be written as:

$$\eta_k\left(\vec{r}+\vec{e}_k dt, t+dt\right)-\eta_k(\vec{r},t)=-\frac{1}{\tau}\left[\eta_k(\vec{r},t)-\eta_k^{eq}(\vec{r},t)\right] \tag{13}$$

where the subscript $k = 0, 1, \ldots, 8$ in the two-dimensional–nine-speed (D2Q9) model shown in Fig. 2. η_k is the distribution function of the discrete velocity at position of $\vec{r}$ and time of t, dt is the time step; τ is the relaxation time, $\vec{e}_k$ is the discrete velocity set, η_k^{eq} is the equilibrium distribution function and generally derived from the Maxwell-Boltzmann distribution of two-dimensional gas (Shi et al., 2004):

$$\eta_k^{eq}=\frac{\rho}{2\pi RT}e^{\left[-\left(\vec{e}_k-\vec{u}\right)^2/2RT\right]} \tag{14}$$

For low *Re* number, Eq. (14) can be expanded as a low-order Taylor series:

$$\eta_k^{eq}=\frac{\rho}{2\pi RT}e^{\left(-\vec{e}_k^{\,2}/2RT\right)\left[1+\frac{\vec{e}_k\vec{u}}{RT}+\frac{1}{2}\left(\frac{\vec{e}_k\vec{u}}{RT}\right)^2-\frac{\vec{u}^2}{2RT}\right]} \tag{15}$$

where R is the gas constant and T is the gas temperature, $\vec{u}$ is the macroscopic velocity.

In the D2Q9 model as shown in Fig. 2, the lattice speed c is defined as $c = \sqrt{3RT}$. Accordingly, Eq. (15) can be written as:

$$\eta_k^{eq}=\frac{\rho}{2\pi RT}e^{\left(-3\vec{e}_k^{\,2}/2c^2\right)\left[1+3\frac{\vec{e}_k\vec{u}}{c^2}+9\frac{\left(\vec{e}_k\vec{u}\right)^2}{2c^4}-\frac{3\vec{u}^2}{2c^2}\right]} \tag{16}$$

The discrete velocity set $\vec{e}_k$ can be expressed as (Yuan and Schaefer, 2006):

$$\vec{e}_k=\begin{cases}(0,0) & k=0\\ (\pm 1,0)c,\ (0,\pm 1)c & k=1,2,3,4\\ (\pm 1,\pm 1)c & k=5,6,7,8\end{cases} \tag{17}$$

Combining Eqs. (16) and (17) yields:

$$\eta_k^{eq}=w_k\rho\left[1+3\frac{\vec{e}_k\vec{u}}{c^2}+9\frac{\left(\vec{e}_k\vec{u}\right)^2}{2c^4}-\frac{3\vec{u}^2}{2c^2}\right] \tag{18}$$

where w_k is the weight coefficient, are given by (Yuan and Schaefer, 2006):

$$w_k=\begin{cases}4/9 & k=0\\ 1/9 & k=1,2,3,4\\ 1/36 & k=5,6,7,8\end{cases} \tag{19}$$

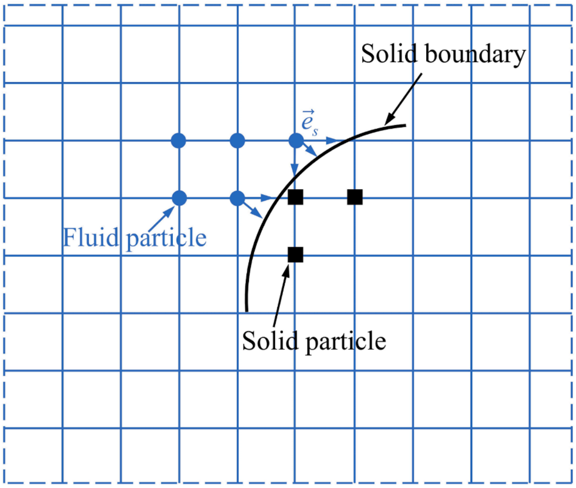

Fig. 3. Graphical illustration of the principle of the momentum exchange method.

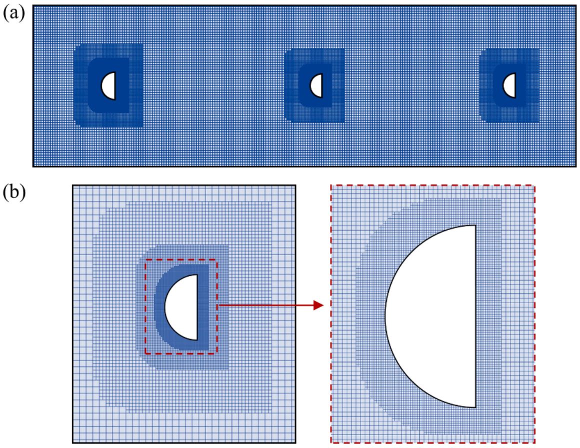

Fig. 4. (a) computational lattice model of the flow field; (b) the enlarged view of the lattice around the semi-circular bluff body.

The macroscopic density ρ, the macroscopic momentum $\rho\vec{u}$ can be obtained from:

$$\rho = \sum_{k=0}^{8} \eta_k = \sum_{k=0}^{8} \eta_k^{eq} \tag{20}$$

$$\rho\vec{u} = \sum_{k=0}^{8} \eta_k \vec{e}_k = \sum_{k=0}^{8} \eta_k^{eq} \vec{e}_k \tag{21}$$

According to Kruger *et al.* (Kruger et al., 2017), $c_s = \sqrt{RT}$ is the speed of lattice sound, and for the incompressible flow with constant temperature T, the macroscopic pressure p can be expressed as:

$$p = \rho RT = \rho c_s^2 \tag{22}$$

where the lattice sound speed is $c_s = c/\sqrt{3}$ in the D2Q9 model.

The acting force of a single node exerted on the solid particle can be calculated by the momentum exchange method, as shown in Fig. 3. $\vec{e}_s$ is the velocity towards the solid boundary. The momentum before a collision is $\vec{e}_s \eta_s(r_f, t)$, and the bounced momentum after a collision is $\vec{e}_s{}' \eta_s(r_f, t + dt)$. Hence, the acting force applied to the solid along the $\vec{e}_s$ direction in one time step is:

$$\vec{F}_s = \left[\vec{e}_s \eta_s\left(r_f, t\right) - \vec{e}_s{}' \eta_s\left(r_f, t + dt\right)\right] \Big/ dt \tag{23}$$

Table 1
Results of domain independence tests in the *y*-direction for simulating the flow past three tandem semi-circular bluff bodies with $d/D = 1.2$ in the forced convective condition at $U_r = 4$.

y– direction height	B1			B2			B3		
	C_D^{mean}	C_L^{rms}	St	Y^{max}	St	Nu_A	Y^{max}	St	Nu_A
27D	1.938	0.472	0.211	0.248	0.176	3.393	0.093	0.176	1.331
30*D*	1.923 (−0.77%)	0.468 (−0.85%)	0.210 (−0.47%)	0.237 (−4.43%)	0.175 (−0.57%)	3.288 (−3.09%)	0.087 (−6.45%)	0.175 (−0.57%)	1.213 (−9.73%)
35*D*	1.921 (−0.10%)	0.465 (−0.64%)	0.209 (−0.47%)	0.234 (−1.26%)	0.175 (0.00%)	3.243 (−1.39%)	0.086 (−1.15%)	0.174 (−0.57%)	1.206 (−0.58%)

Table 2
Results of domain independence tests in the *x*-direction for simulating the flow past three tandem semi-circular bluff bodies with $d/D = 1.2$ in the forced convective condition at $U_r = 4$.

x – direction length	B1			B2			B3		
	C_D^{mean}	C_L^{rms}	St	Y^{max}	St	Nu_A	Y^{max}	St	Nu_A
45*D*	1.927	0.469	0.210	0.241	0.175	3.351	0.091	0.175	1.340
55*D*	1.923 (0.30%)	0.468 (0.99%)	0.210 (0.00%)	0.237 (8.00%)	0.175 (0.00%)	3.289 (−1.85%)	0.087 (−4.60%)	0.175 (0.00%)	1.218 (−9.11%)
65*D*	1.923 (0.00%)	0.468 (0.00%)	0.210 (0.00%)	0.237 (0.00%)	0.175 (0.00%)	3.288 (−0.03%)	0.087 (0.00%)	0.175 (0.00%)	1.213 (−0.41%)

Table 3
Results of different lattice resolutions for simulating the flow past three bluff bodies with $d/D = 1.2$ in the forced convective condition at $U_r = 4$.

Lattice	Number	B1			B2			B3		
		C_D^{mean}	C_L^{rms}	St	Y	St	Nu_A	Y	St	Nu_A
L1	136,125	1.952	0.478	0.210	0.244	0.175	3.158	0.096	0.175	1.311
L2	183,712	1.923 (−1.49%)	0.468 (−2.09%)	0.210 (0.00%)	0.237 (−2.87%)	0.176 (0.57%)	3.291 (4.21%)	0.087 (−9.38%)	0.175 (0.00%)	1.218 (−7.09%)
L3	230,019	1.918 (−0.26%)	0.464 (−0.85%)	0.209 (−0.48%)	0.236 (−0.42%)	0.175 (−0.57%)	3.311 (0.61%)	0.086 (−1.15%)	0.174 (−0.57%)	1.222 (0.33%)

where $\vec{e}_s{}'$ is the velocity after a collision. Then, the total acting force at the $\vec{e}_s$ direction applied to the solid in one time step can be written as:

$$\vec{F}_t = \sum_{s=0}^{9}\sum_{f=0}^{9}\vec{F}_k = \left[\vec{e}_s\eta_s(r_f,t) - \vec{e}_s{}'\eta_s(r_f,t+dt)\right] \Big/ dt \tag{24}$$

3.2. Lattice generation and independence study

Mesh and time-step dependency studies are performed for the WIV of three tandem semi-circular cylinders at $d/D = 1.2$ and $U_r = 4$ to ensure convergent results. The computational domain consists of mutually orthogonal lattices. Three lattice models (coarse – L1 model, normal – L2 model, fine – L3 model) with different lattice numbers (136,125, 183,712, 230,019) are compared. The most refined lattice that is uniformly distributed around the bluff body has a size of 0.016*D* and moves continuously with the movement of the bluff body. The two-part lattice transition region is set to achieve smooth computational results. The lattice model is adequately refined to capture the viscous boundary layer (Darbhamulla and Bhardwaj, 2021), and the lattice structure of the flow field is shown in Fig. 4.

The time-averaged drag coefficient C_D^{mean}, root-mean-square (RMS) lift coefficient C_L^{rms}, Strouhal number St, the time-averaged Nusselt number Nu_A, and the dimensionless transverse vibration amplitude Y^{max} are compared in the independence verification of computational domain, grid density, and time step.

By comparing the data under different *y*-direction heights *H* (27*D*, 30*D*, 35*D*) in Table 1 and different *x*-direction lengths *L* (45*D*, 55*D*, 65*D*) in Table 2, the optimal computational domain size is identified as $L \times H = 30D \times 55D$. Thus, the minimum distance between B3 and the outlet boundary is 25.4*D*, and the maximum cross-flow block ratio is $1.4D/30D = 4.67\%$, which can satisfy the requirement of a block ratio of less than 5% (H. Zhu et al., 2022; Zafar and Alam, 2018).

For the different lattice models listed and compared in Table 3, the maximum error between L2 and L3 does not exceed 1.15%. Considering the computational cost, the normal lattice model (L2) is adopted in the following studies.

Based on the selected L2 model, three different time steps (0.016s, 0.012s, 0.008s) are studied to ensure the convergence of the

Table 4
Results of different time steps for simulating the flow past three bluff bodies with $d/D = 1.2$ in the forced convective condition at $U_r = 4$ using L2 lattice scheme with a lattice number of 183,712.

dt	B1			B2			B3		
	C_D^{mean}	C_L^{rms}	St	Y	St	Nu_A	Y	St	Nu_A
0.016s	1.961	0.487	0.211	0.251	0.175	3.375	0.112	0.175	2.288
0.012s	1.923 (−1.94%)	0.468 (−3.90%)	0.211 (0.00%)	0.237 (−5.58%)	0.176 (0.57%)	3.292 (−2.46%)	0.087 (−22.32%)	0.176 (0.57%)	1.218 (−46.76%)
0.008s	1.929 (0.31%)	0.465 (−0.64%)	0.210 (−0.47%)	0.236 (−0.42%)	0.175 (−0.57%)	3.314 (0.67%)	0.085 (−2.30%)	0.175 (−0.57%)	1.220 (0.16%)

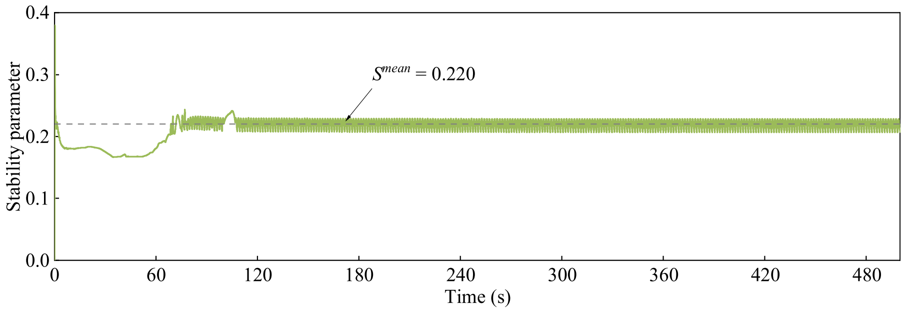

Fig. 5. The stability parameter S for simulating the flow past three bluff bodies with $d/D = 1.2$ in the forced convective condition at $U_r = 4$.

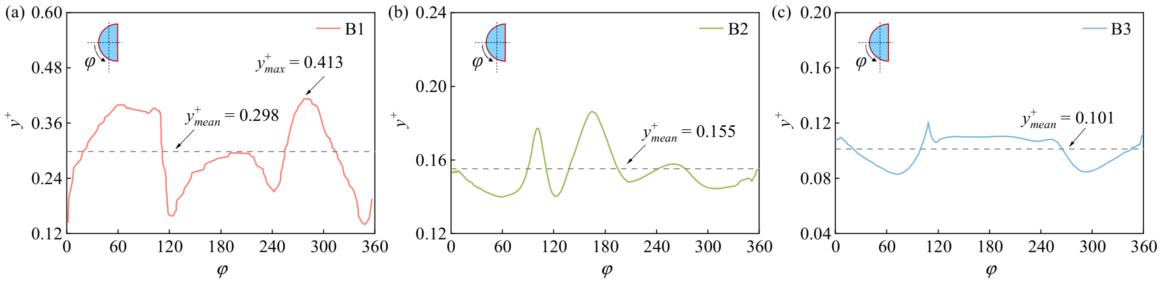

Fig. 6. The time-averaged y^+ of B1, B2, and B3 for simulating the flow past three bluff bodies with $d/D = 1.2$ in the forced convective condition at $U_r = 4$.

result. The results are listed in Table 4. The maximum error margin between $dt = 0.012$s and $dt = 0.008$s is less than 2.3%. Therefore, $dt = 0.012$s is selected for the following simulations. The other d/D situations in the following studies will use a similar lattice number as the L2 model.

In general, the stability parameter S is a significant criterion that can justify the solution stability. In XFlow, S is defined as:

$$S = \frac{max(S_v, S_{nu}, S_\rho)}{0.7} \tag{25}$$

The stability parameter S should strictly satisfy the Courant–Friedrichs–Lewy (CFL, S_v) condition, compressibility (S_ρ) condition, and numerical viscosity (S_{nu}) condition, and its value must be less than 1. S_ρ, S_{nu}, S_v can be expressed as:

$$S_\rho = \frac{2(\rho_{max} - \rho_{min})}{(\rho_{max} + \rho_{min})}, S_{nu} = \frac{\nu}{C_s dx}, S_v = \frac{U_{max} dt}{dx} \tag{26}$$

where dx is the resolution at a given lattice level, and dt is the associated time step for the same lattice level.

As shown in Fig. 5, the built-in stability parameter S provided by XFlow is smaller than 0.4 to keep the Courant number smaller than 1.0. It can be seen that S is keeping around 0.2–0.3 during the simulation, and the time-averaged stability parameter S^{mean} is equal to 0.220. As a consequence, it can be declared that the numerical method is acceptable.

The second criterion is y^+, y^+ is the dimensionless distance from the wall, and it is defined as:

$$y^+ = \frac{\rho v_\tau y_1}{\mu}, v_\tau = \sqrt{\frac{\tau_w}{\rho}}, \tau_w = \mu\left(\frac{\partial v}{\partial y}\right)_{y=0} \tag{27}$$

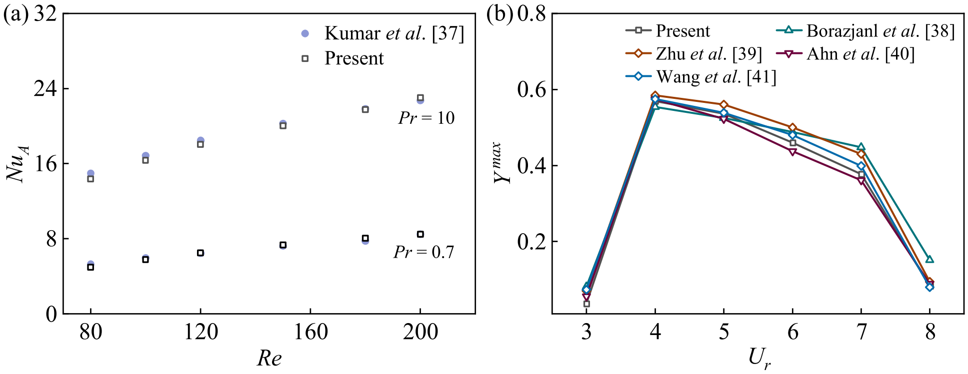

Fig. 7. Validation of the implemented numerical algorithm: (a) flow past a fixed semicircle bluff bodies in the forced convection condition at $Pr =$ 0.7 and 10; (b) flow past a single-degree-of-freedom circular cylinder over $U_r = 3$–8 at $Re = 150$, $m^* = 2$, $\zeta = 0$.

Table 5
Comparison of the present simulation result with the results from the literature and calculated by the empirical formula for the flow around a stationary heated circular cylinder at different *Re*.

Re	Literature	C_D^{mean}	C_L^{rms}	St	Nu_A
150	Present	1.354	0.362	0.183	6.555
	Zafar *et al.* (Zafar and Alam, 2019)	1.349	0.353	0.183	6.386
	Izadpanah *et al.* (Izadpanah et al., 2018)	1.355	0.378	0.187	6.395
	Eq. (28)				6.393
200	Present	1.347	0.489	0.190	7.589
	Mahír *et al.* (Mahír and Altaç, 2008)	1.376	0.496	0.192	7.474
	Ding *et al.* (Ding et al., 2022)	1.348	0.466	0.196	/
	Eq. (28)				7.376

where v_τ is the friction velocity at the wall, y_1 is the distance from the first lattice to the wall, and τ_w is the wall shear stress. It is recommended to keep y^+ under 0.5 at $Re < 300$. As shown in Fig. 6, the time-averaged $y^+{}_{mean}$ is smaller than 0.375 (H. Zhu et al., 2022), and the max y^+ never exceeds 0.42. Therefore, we can state that the choices of domain, grid, and time step size are reasonable in the present study.

3.3. Model validation

This section will validate the simulation method through a reference model from the literature. In the first case, as shown in Fig. 7 (a), the flow around the stationary semi-circular cylinder at different *Re* is investigated ($Pr = 0.7$ and 10). The computed Nu_A values are compared with those in the literature (Kumar et al., 2016). In the second case, as shown in Fig. 7(b), a single-degree-of-freedom (SDOF) cylinder ($m^* = 2$ and $\zeta = 0$) vibrating in the transverse direction at $Re = 150$ is studied. The dimensionless transverse vibration amplitude Y^{max} is compared over $U_r = 3$–8 (Borazjani and Sotiropoulos, 2009; H.J. Zhu et al., 2020; Ahn and Kallinderis, 2006; Wang et al., 2016).

The third case investigates the flow around a fixed heated circular cylinder at different *Re*. The results are listed in Table 5. The time-averaged Nusselt number is also compared with the empirical formula derived by Churchill *et al.* (Churchill and Bernstein, 1977). It can be expressed as:

$$Nu_A = 0.3 + \frac{0.62Re^{1/2}Pr^{1/3}}{\left[1 + (0.4/Pr)^{2/3}\right]^{1/4}}\left[1 + \left(\frac{Re}{28200}\right)^{5/8}\right]^{4/5} \tag{28}$$

The three validation cases are in good agreement with those in the literature. Therefore, it can be declared that the numerical scheme used in this study has achieved an acceptable level of accuracy.

4. Results and discussions

4.1. Wake interference pattern and evaluation

Based on the four wake interference patterns proposed by Zhu *et al.* (Zhu and Wang, 2019; Zhu et al., 2021), only two wake patterns are observed between adjacent bluff bodies: the quasi-co-shedding (QCS) pattern and the co-shedding (CS) pattern. Moreover, the coupling between QCS and CS (QCS-CS) patterns was observed in some situations, preserving the typical characteristics of QCS and CS

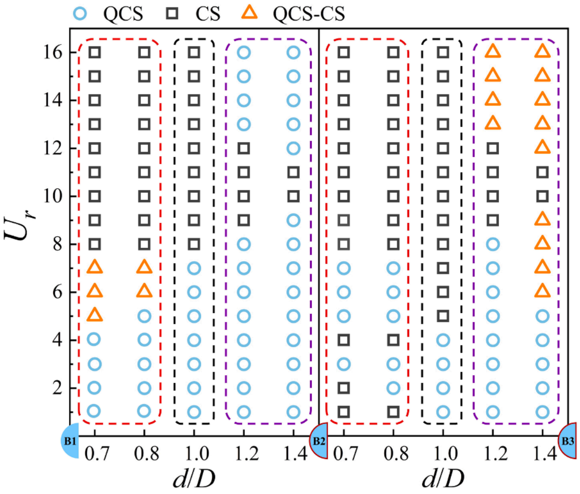

Fig. 8. Three wake interference patterns of two vibrating bluff bodies: QCS denotes the quasi-co-shedding pattern, CS denotes the co-shedding pattern, and QCS-CS denotes the coupling of QCS and CS pattern.

patterns. Fig. 8 presents three wake interference patterns observed in this study as d/D and U_r increase. According to the distribution of different wake interference patterns, the five diameter ratios have been divided into three categories: $d/D = 0.7$ and 0.8 are the first category; $d/D = 1.0$ is the second category; $d/D = 1.2$ and 1.4 are the third category. To avoid redundancy, representative d/D values ($d/D = 0.8$, 1.0, and 1.4) have been chosen to interpret the wake interference patterns. As shown in Fig. 9(e), at $d/D = 1.4$ and $U_r = 2$, vortices alternatively shed off from B1, forming a double-row vortex at the midstream. In this case, the vortex generation of the B2 is inhibited, the vortices shed off from B2 become much less. Hence, it is called the QCS pattern. Different patterns are observed at $d/D = 1.0$ and $U_r = 10$ in Fig. 9(c), vortices also alternatively shed off from B1 but cannot inhibit the vortex generation of B2 and B3, the vortices generated by the upstream and midstream bluff bodies can either move downstream or blend with other vortices, resulting in more vortices and different vortex-shedding states for the three bluff bodies, thus, it is called the CS pattern. Another wake interference pattern is observed in Fig. 9(e) for the case of $d/D = 1.4$, $U_r = 6$, and $U_r = 14$, the vortices shed off from B1 and flow around B2, most of the evolved vortices flow around B3, resulting in a small number of vortices generated behind B3, the vortex-shedding of B3 is in a partially inhibited state. Thus, this pattern is termed the QCS-CS pattern.

It can be seen from Fig. 9 that the center width of the vortex core of B1 basically increases with the increase of d/D, which also makes the wake interference pattern between B1 and B2 obviously different under different d/D. When $d/D = 0.7$ and $U_r = 1$–7, two patterns are found between B1 and B2. It can be inferred that B1 is too small to produce wider wake vortices, the width of wake vortices is $0.66D$ when $U_r = 2$, and the streamwise spacing between B1 and B2 is too limited, so the wake vortices cannot evolve to a double-row state before colliding with B2, resulting a CS-like pattern between B1 and B2 at low U_r. Essentially, the vortex shed by B1 directly collides on the surface of B2 and then sheds from the surface of B2 again. Rather than directly flowing around B2, the vortex generation of B2 is suppressed, so it still belongs to the QCS pattern. When $U_r = 6$–7, the amplitude of B2 increases and pushes the upstream vortices to the sides of B2, resulting in the QCS-CS pattern between B1 and B2, and this phenomenon gradually transforms as d/D increases.

When $d/D = 0.8$ and $U_r = 8$–16, the wake interference pattern between B1 and B2 changes to CS again because the reduction of transverse vibration amplitude of B2 breaks the evolving process of the vortices generated by B1 and the vortices collide with B2 again, the width of wake vortices is still narrow, e.g., when $d/D = 0.8$ and $U_r = 10$, 14, the center widths of B1 wake vortices are $0.81D$ and $0.91D$, respectively. The patterns between B2 and B3 in the case of $d/D = 0.8$ and $U_r = 5$-7 are different to B1 and B2. When $U_r = 6$–7, the vortices in front of B3 are fully developed and have enough width to flow around B3 and a more obvious QCS pattern between B2 and B3 occurred despite B3 shows a larger transverse vibration amplitude. For $d/D = 0.7$ and 0.8 at $U_r = 1$–4, the width of the vortex street slightly increases behind B2, and due to the complex vortex interaction behind B2, the CS patterns can more easily occur between B2 and B3 than in other cases over $U_r = 1$–4.

When $d/D = 1.0$, three bluff bodies have the same diameter, and B1 has enough diameter to produce a wide vortex street, e.g., the center width of wake vortices is $1.02D$ when $U_r = 2$. In this case, no obvious CS pattern between B1 and B2 occurs when $U_r < 8$. Then, the pattern between B1 and B2 changes to CS when $U_r > 8$ because the transverse vibration amplitude of B2 is suddenly increased. The CS pattern between B2 and B3 occurs when $U_r > 4$ because B3 has a larger transverse vibration amplitude than B2.

When $d/D = 1.4$, with further increase of the diameter of B1, the wake generated by B1 has enough width to flow around B2, e.g., the center widths of wake vortices are $1.88D$ when $U_r = 2$ and $1.80D$ when $U_r = 6$, the spacing between B1 and B2 is enough for the vortices to fully evolve into a double-row vortex street in the streamwise direction. Therefore, the CS pattern between B1 and B2 only appears at $U_r = 10$ and $U_r = 11$ due to the large transverse amplitude of B2, and the QCS pattern occurs when $U_r = 1$–9 and $U_r = 12$–14. The pattern between B2 and B3 is similar to that between B1 and B2. A more obvious QCS-CS pattern between B2 and B3 occurs when $U_r = 6$–9 and $U_r = 13$–16 because vortices behind B3 transform into weaker vortices. For $d/D = 1.2$, the CS pattern between B1 and B2

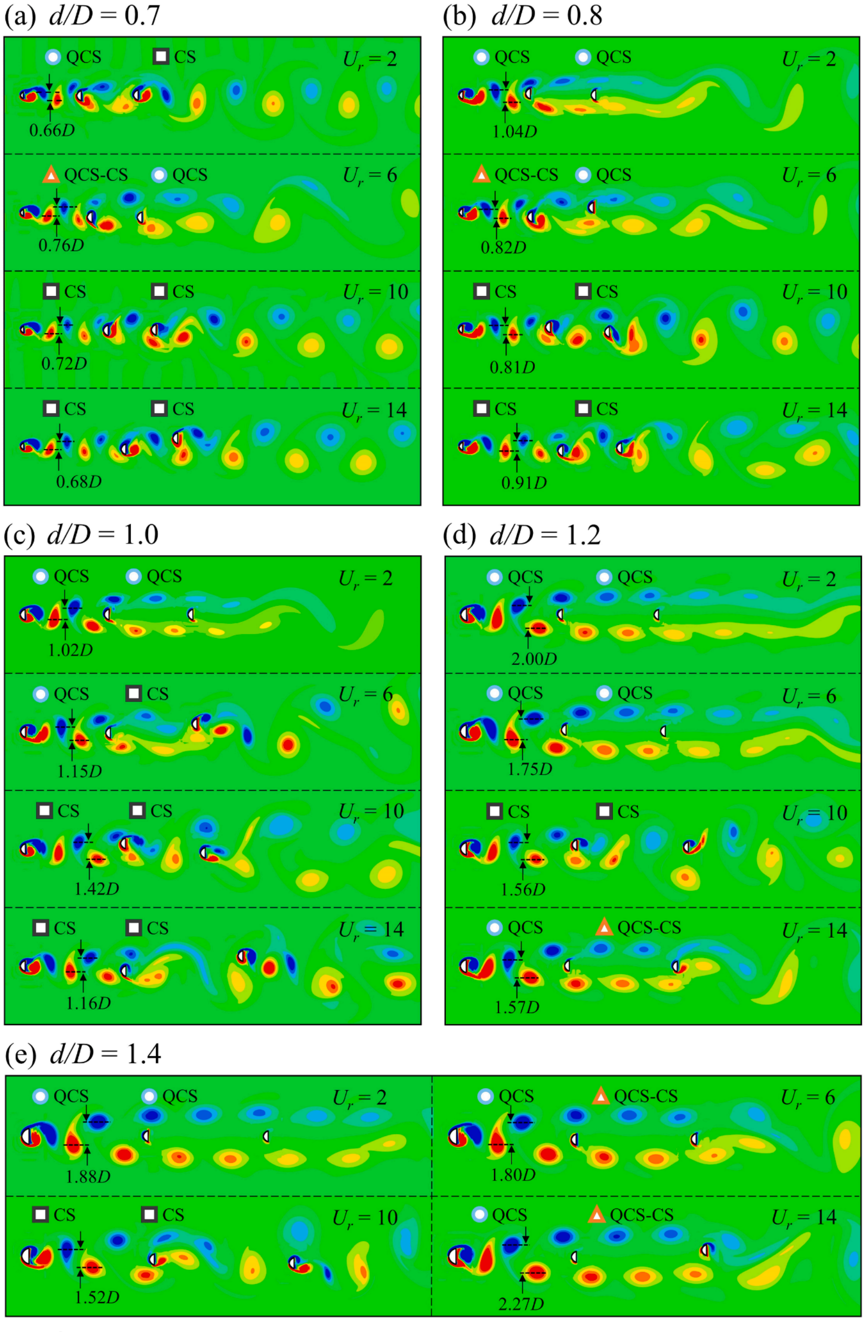

Fig. 9. Vortex structure and wake interference pattern at $U_r = 2, 6, 10, 14$ for different d/D: (a) $d/D = 0.7$; (b) $d/D = 0.8$; (c) $d/D = 1.0$; (d) $d/D = 1.2$; (e) $d/D = 1.4$.

is observed at $U_r = 9$–12 because the high transverse amplitude of B2 breaks the normal movement of vortices. The QCS pattern between B1 and B2 is observed at $U_r = 1$–8 and $U_r = 13$–16 because the lower transverse amplitude cannot break the normal vortex movement. In the downstream region of B2 and B3, the QCS-CS pattern is observed at $U_r = 13$–16, unlike the case of $d/D = 1.4$, the QCS pattern between B2 and B3 occurs at $U_r = 1$–8 due to the lower transverse amplitude of B3. The CS pattern between B2 and B3 occurs at $U_r = 9$–12 due to the increased transverse amplitude of B3.

As we can see in Fig. 8 and Fig. 9, most QCS-CS patterns appear between B2 and B3 because the streamwise spacing between B1 and B2 is not large enough for the vortices to evolve fully. On the contrary, the streamwise spacing behind B3 is quite large, which is

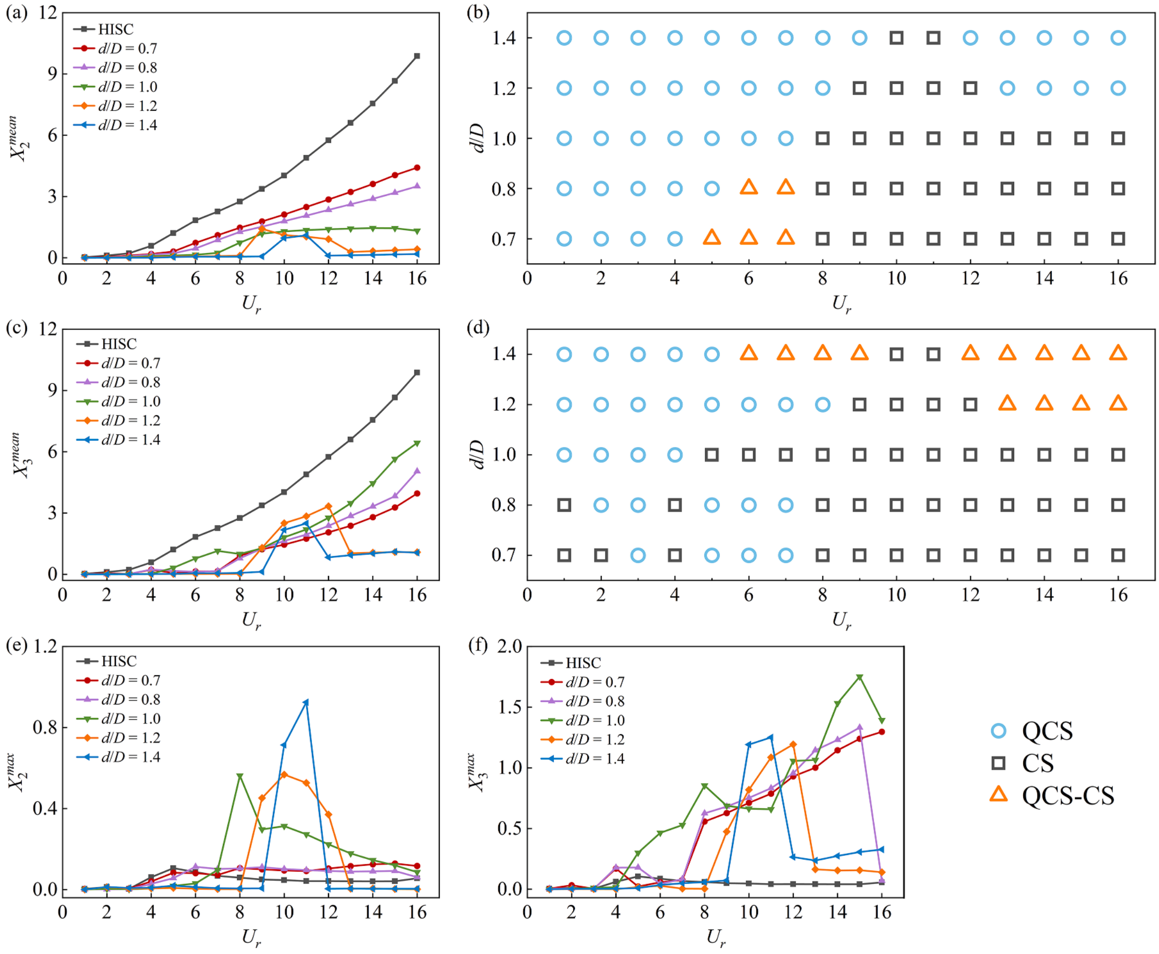

Fig. 10. The dimensionless time-averaged streamwise displacement of B2 and B3 and the corresponding dimensionless streamwise vibration amplitudes: (a)&(e) B2; (c)&(f) B3. Subfigures (b)&(d) are the wake interference patterns to give a clear comparison of X^{mean} and X^{max}.

conducive to the emergence and evolution of vortices.

4.2. Wake-induced vibration and frequency response

In this section, the structural dynamics of B2 and B3 are studied. During the WIV process, the wake flow and the heat transfer of the bluff body are significantly affected because it vibrates freely in two directions. At the same time, the coupling between the fluid dynamics and the heat transfer under the forced convection also induces strong nonlinearity, making the dynamic analysis complicated. In particular, the thermal convection efficiencies (Nu) around B2 and B3 are greatly influenced by the mutual interference between the flow wake and structural dynamics response during the heat convection process. In a word, the WIV of the tandem bluff body is a highly nonlinear thermal-fluid-structure coupling problem.

First of all, Fig. 10 presents the variations of the dimensionless averaged streamwise displacements X^{mean} and the dimensionless streamwise vibration amplitude X^{max} of B2 and B3 versus U_r at different d/D. In this section, we cluster the wake interference patterns in Fig. 10 to give a clear comparison. The VIV response of a heat-isolated semi-circular cylinder (HISC) with the same dimensionless parameters ($Re = 200$, $m^* = 2.0$, $U_r = 1$–16, $\zeta = 0$) is taken as the baseline for comparison. X^{mean} and X^{max} can be defined as:

$$X^{mean} = \frac{1}{N}\sum_{i=1}^{N} X_i \tag{29}$$

$$X^{max} = \sqrt{\frac{2}{N}\sum_{i=1}^{N}\left(X_i - X^{mean}\right)^2} \tag{30}$$

where N is the number of the values in the time series for statistics, and i starts from a relatively stable vibration period.

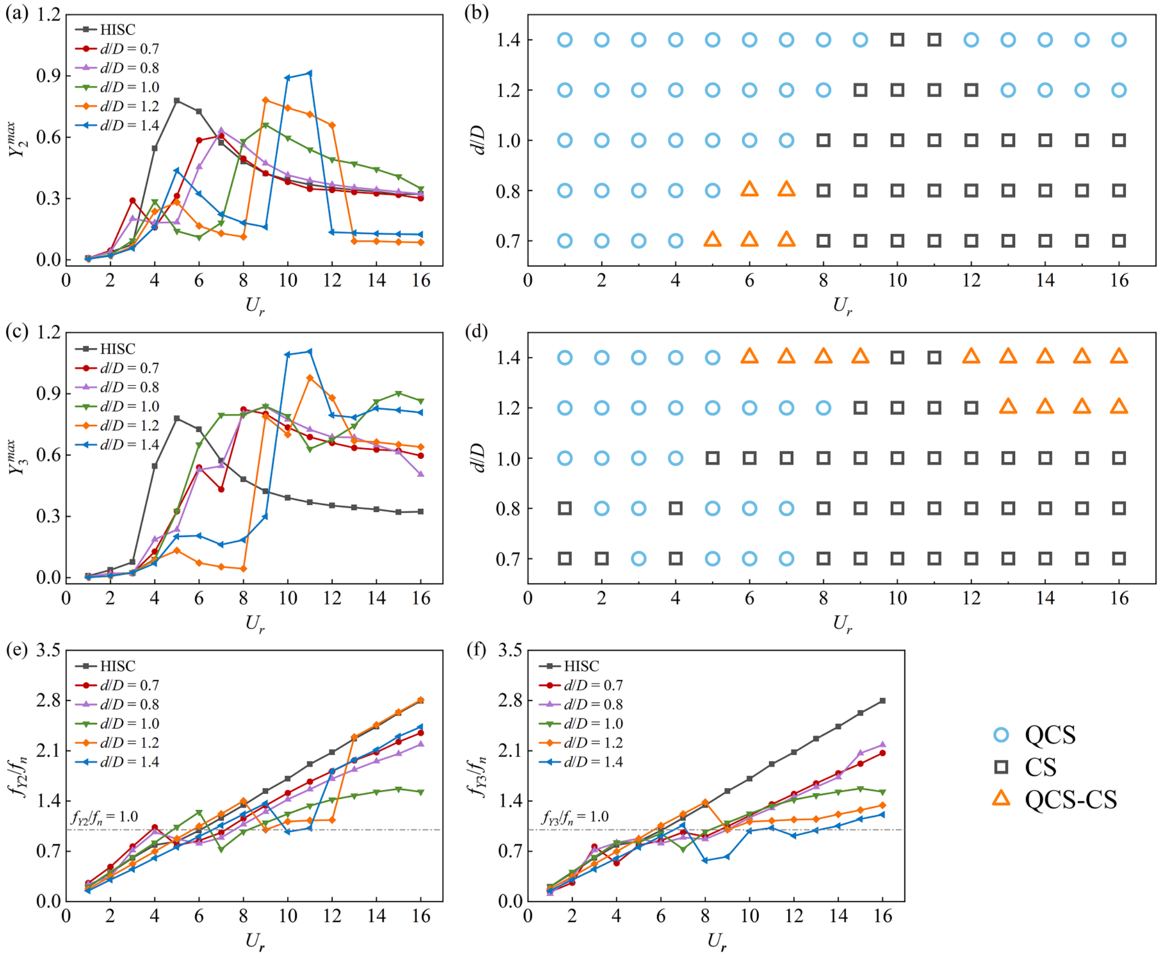

Fig. 11. Transverse vibration responses of B2 and B3 and the corresponding frequency ratios: (a)&(e) B2; (c)&(f) B3. Subfigures (b)&(d) are the wake interference patterns to give a clear comparison with Y^{max}.

For the HISC, X^{mean} increases with U_r. It exhibits a slight and slow increase when $U_r = 1$–3 and a monotonic increase when $U_r =$ 4–16. The maximum X^{mean} of the HISC is achieved at $U_r = 16$. Putting aside the HISC, we first discuss the response of B2 and B3, i.e., ${X_2}^{mean}$ and ${X_3}^{mean}$. For $d/D = 0.7$ and 0.8, ${X_2}^{mean}$ is basically consistent with that of the HISC. The monotonic increase of ${X_2}^{mean}$ occurs when $U_r = 6$–16, and the maximum ${X_2}^{mean}$ dramatically decreases due to the partial 'blocking effect' of B1. Theoretically, compared with ${X_2}^{mean}$, ${X_3}^{mean}$ should sharply reduce due to the blocking effects of B1 and B2. However, according to Fig. 9(a) and Fig. 9(b), the vortices generated by B1 and B2 have large impacts on B3 under the CS pattern. Therefore, a similar change takes place in ${X_3}^{mean}$ compared with ${X_2}^{mean}$. The monotonic increase of ${X_3}^{mean}$ is observed at $Ur = 7$–16. For $d/D = 1.0$, with the diameter of B1 further increasing, the blocking effect of B1 on the downstream also strengthens. Thus, there is no significant increase in ${X_2}^{mean}$. The wake interference between B1 and B2 changes to the CS pattern when $U_r > 8$, and ${X_2}^{mean}$ starts to increase after $U_r = 8$, then keeps almost stable between $U_r = 10$–16. ${X_3}^{mean}$ is small within $U_r = 1$–4 because of the QCS pattern between B2 and B3. Due to the switch of the wake interference pattern, the vortices generated by B1 and B2 have more obvious promotion effects on B3 than in the case of $d/D =$ 0.7 and 0.8, as revealed in Fig. 9 and Fig. 10(b). Consequently, ${X_3}^{mean}$ increases monotonically. In the cases of $d/D = 1.2$ and $d/D = 1.4$, ${X_2}^{mean}$ and ${X_3}^{mean}$ are quite different from the other three cases. Due to the strong blocking effect of B1, ${X_2}^{mean}$ and ${X_3}^{mean}$ can no longer maintain a monotonic growth or stable state. A VIV-like 'lock-in' region (Prasanth and Mittal, 2007; J.L. Wang et al., 2020) appears over $U_r = 9$–12 when $d/D = 1.2$ and $U_r = 10$–11 when $d/D = 1.4$. For $d/D = 1.2$, the wake interference changes to CS over $U_r = 9$–12. For $d/D = 1.4$, the CS pattern occurs only within $U_r = 10$–11.

Note that X^{mean} represents the position of the bluff body deviating from the original point. As we can conclude from Fig. 8 and Fig. 10, for different d/D, a larger X^{mean} indicates a greater occurrence probability of the CS pattern.

In addition, Fig. 10 shows that X^{max} of the HISC is relatively small compared with the other cases. The X^{max} of HISC starts to increase at $U_r = 4$, and finally starts to decrease slightly when $U_r > 5$. It can be treated as an unobvious 'lock-in' region of the HISC. For $d/D =$ 0.7 and 0.8, the variation of ${X_2}^{max}$ is nearly consistent with the HISC but shows a little difference. ${X_2}^{max}$ shows a stable state after $U_r =$ 4. For $d/D = 1.0$, the variation of ${X_2}^{max}$ is quite different compared with the cases of $d/D = 0.7$ and 0.8. There is no noticeable increase

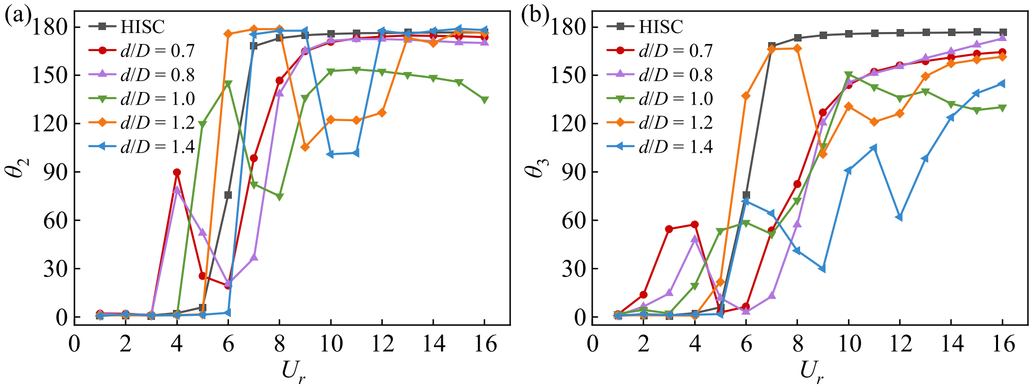

Fig. 12. The phase difference between the lift coefficient and the transverse vibration amplitude at different d/D: (a)B2; (b)B3.

when $U_r = 1$–6, and a sudden increase occurs over $U_r = 7$–8. At the same time, the wake interference changes from QCS to CS pattern. X_2^{max} starts to decrease when $U_r = 9$. According to its profile, it can be deemed as an obvious 'lock-in' region. For $d/D = 1.2$ and 1.4, the 'lock-in' region is observed over $U_r = 8$–13 at $d/D = 1.2$ and $U_r = 10$–11 at $d/D = 1.4$. Also, the 'lock-in' region becomes more pronounced.

As shown in Fig. 10(b), the variation of X_3^{max} is remarkably different compared with X_2^{max}. For most cases, X_3^{max} shows a growing trend. For $d/D = 0.7$ and 0.8, a considerable increase occurs at $U_r = 8$ because the wake interference changes to the CS pattern at $U_r = 8$. A monotonic increase is observed for $d/D = 0.7$ over $U_r = 8$–16, and a dramatic decrease is observed for $d/D = 0.8$ at $U_r = 16$. A wide 'lock-in' region is formed between $U_r = 8$–16, and the CS pattern is maintained over this range. For $d/D = 1.0$, an X_3^{max} increasing trend is observed when $U_r = 5$–16 and the CS pattern occurs at $U_r = 5$. For $d/D = 1.2$ and 1.4, there is still an obvious 'lock-in' region over the same U_r range as in Fig. 11(a). Since the vortex evolution becomes more complex in the region closer to the downstream, X_3^{max} is also larger than X_2^{max} at higher U_r. It can be concluded from Fig. 8 to Fig. 11 that a larger X^{mean} or X^{max} can induce the wake interference pattern to change from QCS to CS.

The transverse vibration amplitude of the bluff body Y^{max} is also another important parameter for studying the dynamics of WIV, and it is often associated with the frequency ratio f/f_n, where f is the vibration frequency. It can be obtained by fast Fourier transform (FFT) of the displacement time histories. Because both the midstream and downstream bluff bodies are immersed in the wake behind the upstream cylinder, with the diameter of the upstream bluff body increases, the structural dynamics are more severely perturbed by the shear layers and vortices produced by the upstream bluff body, making the problem more complicated than the HISC. As shown in Fig. 12, a typical VIV is observed for the HISC, and its structural dynamics can be classified into three distinct branches: the initial branch (IB), the lower branch (LB), and the desynchronization branch (DB) (Zhu and Liu, 2020). The IB branch is within the range $U_r = 1$–4, the LB branch is within the range $U_r = 5$–7, and the DB branch occurs over $U_r = 8$–16, as demonstrated in Fig. 12(a) and Fig. 12(b). The 'lock-in' region can be determined to be over $U_r = 4$–7. The front and rear parts of the HISC have the nature of a cylinder and a square, respectively. It leads to the HISC keeping a larger amplitude in the DB region. The HISC still exhibits VIV over the whole U_r range, and the maximum Y^{max} is 0.78 at $U_r = 5$.

For the other cases, we can also classify them into three groups according to the variation of transverse vibration amplitude for the midstream bluff body B2. According to Fig. 11(a) and Fig. 11(b), a small IB region is observed over $U_r = 1$–3 for $d/D = 0.7$ and 0.8, then the vibration amplitude increases over $U_r = 4$–6. The Y_2^{max} of $d/D = 0.7$ and 0.8 is pretty similar with HISC in the range of $U_r = 7$–16. An LB region is within the range $U_r = 7$–8, and a DB branch occurs over $U_r = 9$–16. The 'lock-in' region can be determined over $U_r = 3$–4 and $U_r = 6$–8 because the frequency ratio is close to 1.0. The two switches of wake interference pattern between B1 and B2 are observed when $d/D = 0.7$ and 0.8. The maximum Y_2^{max} of the cases having $d/D = 0.7$ and 0.8 are 0.61 and 0.63, respectively, at $U_r = 7$. For $d/D = 1.0$, a small IB region is observed over $U_r = 1$–4, followed by a high increment of Y_2^{max} over $U_r = 6$–8. It is not easy to directly distinguish the LB and DB regions for $d/D = 1.0$ over $U_r = 9$–16 in Fig. 11(a). But as shown in Fig. 11(b), according to the frequency ratio, we can identify that the LB region is within the range of $U_r = 8$–10, and the DB region spans over $U_r = 11$–16. The 'lock-in' region for $d/D = 1.0$ can be determined to be $U_r = 4$–5 and 8–10. the only one switch of wake interference pattern between B1 and B2 are observed at $Ur = 8$. The maximum Y_2^{max} is 0.66 at $U_r = 9$. The results for $d/D = 1.2$ and $d/D = 1.4$ are pretty different from the other three cases and the HISC at high U_r. When U_r is low, a small IB region forms over $U_r = 1$–5 for $d/D = 1.2$ and 1.4, The LB region over $U_r = 9$–12 and the DB region over $U_r = 13$–16 are also identified for $d/D = 1.2$. A narrower DB region over $U_r = 11$–12 and a wider LB region over $U_r = 12$–16 are observed for $d/D = 1.4$. Therefore, we can conclude that the 'lock-in' regions occur over $U_r = 5$–6 and $U_r = 9$–12 for $d/D = 1.2$; $U_r = 5$–7 and $U_r = 10$–11 for $d/D = 1.4$. The maximum $\mathrm{Y}_2^{\max}$ are 0.78 and 0.91 for the cases with $d/D = 1.2$ and 1.4, respectively.

The transverse vibration amplitude of B3 (Y_3^{max}) is pretty different from B2. Generally, due to the perturbation of the upstream vortices, Y_3^{max} further increases. As shown in Fig. 11(c), the downstream B3 shows large vibration amplitudes at high U_r compared with HISC, even though the frequency ratio significantly deviates from 1.0. According to Chen *et al.* (Chen et al., 2018), it seems that the frequency criterion is inapplicable to define the 'lock-in' region of B3. Prasanth *et al.* (Prasanth and Mittal, 2009) and Borazjani *et al.* (Borazjani and Sotiropoulos, 2009) suggested that the region with high vibration amplitude is the 'lock-in' region. It is totally

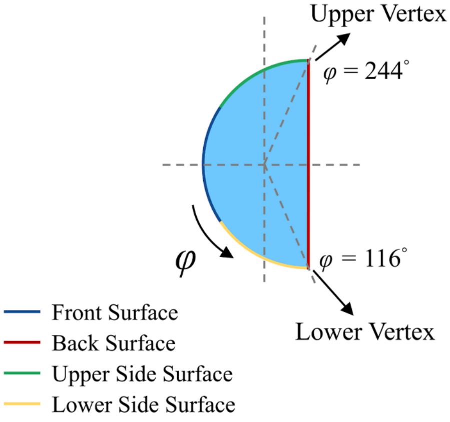

Fig. 13. Semi-circular cylinder surface partition, e.g., back surface $\varphi = 116^\circ - 244^\circ$.

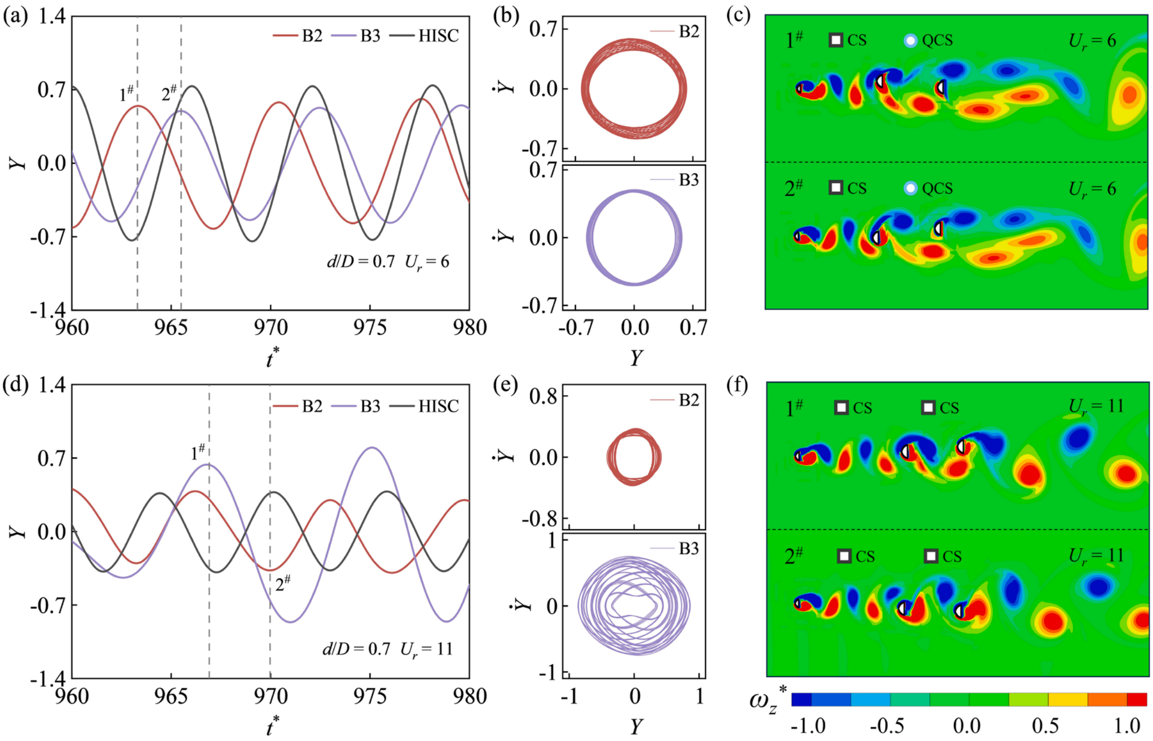

Fig. 14. The displacement time histories, phase plots, and vorticity contours of three tandem semi-circular cylinders at $d/D = 0.7$ and different U_r: (a)&(d) the displacement time histories of B2 and B3 at $U_r = 6$, 11; (b)&(e) the phase plots of B2 and B3; (c)&(f) the vorticity contours.

different compared with B2 and HISC. Therefore, we no longer define the LB and DB of B3 because B3 has a much wider 'lock-in' region than B2, and the vibration response of B3 is more complex than B2 and HISC.

For $d/D = 0.7$ and 0.8, an IB region is observed over $U_r = 1$–8, as demonstrated in Fig. 11(c)&(d). The wake interference changes to the CS pattern after $U_r = 8$. The wake interference changes to the CS pattern after $U_r = 8$ when $d/D = 0.7$ and $U_r = 6$ when $d/D = 0.8$. The maximum $Y_3{}^{max}$ for $d/D = 0.7$ and 0.8 is 0.82 and 0.84, respectively, at $U_r = 8$. The 'lock-in' region can be determined to be $U_r =$ 8–16. For $d/D = 1.0$, B3 keeps a high vibration amplitude after $U_r = 7$, although it slowly decreases over $U_r = 9$–11, then increases again after $U_r = 11$. Hence, we can conclude that the 'lock-in' region is over $U_r = 6$–16. The wake interference changes to the CS pattern after $U_r = 5$, and the maximum $Y_3{}^{max}$ is 0.90 at $U_r = 15$. As the distance between the bluff bodies further increases for the case of $d/D =$ 1.2, the vortices have sufficient space to evolve. The vortex intensity reduced significantly in front of B3, and the vortex street is too wide to change the wake interference pattern at low U_r. Until $U_r = 9$, the high vibration amplitudes of B2 and B3 disturb the vortex street and change to the CS pattern. Over $U_r = 13$–16, B2 is basically stationary. However, the large amplitude vibration of B3 destroys the fully developed vortex streets from B1 and B2. Thus, the wake interference turns into the QCS-CS pattern. For $d/D = 1.4$, the

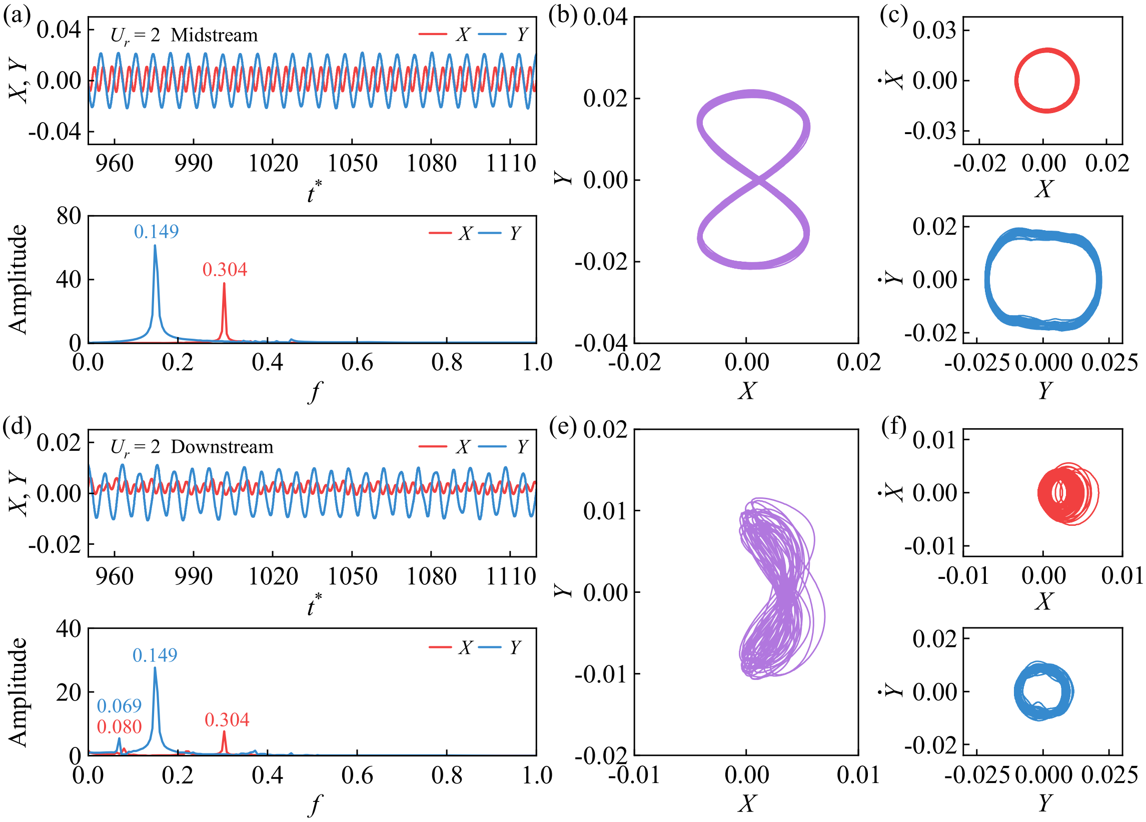

Fig. 15. The displacement time histories and the frequency contours, trajectories, and phase plots of the midstream (B2) and downstream (B3) bluff bodies at $U_r = 2$: (a)&(d) displacement time histories; (b)&(e) trajectories; (c)&(f) phase plots.

intensity of the vortex decreases when it reaches downstream. A slightly larger vibration amplitude of ${Y_3}^{max}$ causes the wake interference between B2 and B3 to change from the QCS to QCS-CS pattern over $U_r = 6$–9, then transforms into the CS pattern between B2 and B3 over $U_r = 10$–11 due to the extremely high amplitude of B2 and B3. The wake interference between B2 and B3 changes to the QCS-CS pattern over $U_r = 12$–16 due to the stationary state of B2 and the high amplitude vibration of B3. The maximum ${Y_3}^{max}$ for $d/D = 1.2$ and 1.4 are 0.98 and 1.11, respectively, at $U_r = 11$.

Combining the information in Fig. 8 and Fig. 11, it can be inferred that both B2 and B3 should have large transverse amplitudes to induce the wake interference changing into the CS pattern at higher U_r. Moreover, reducing the distance between two vortex streets, which means reducing the diameter d of B1, can also help the wake interference change to the CS pattern.

Then, the phase difference θ between the RMS lift coefficient C_L^{rms} and the transverse displacement of Y for B2 and B3 at $d/D = 1.4$ are investigated to figure out the correlation between C_L^{rms} and Y. C_L^{rms} is defined as:

$$C_L^{rms} = \sqrt{\frac{1}{N}\sum_{i=1}^{N}\left(\frac{2F_L^i}{\rho U_\infty^2 D}\right)^2} \tag{31}$$

where F_L^i is the lift force, and i starts from a stable vibration period. θ can be calculated by using the Hilbert transform (Kareem and Kijewski, 2002), and the results are shown in Fig. 12. When $\theta = 0^\circ$, C_L^{rms} and Y are in phase; when $\theta = 180^\circ$, the C_{Lrms} and Y are in reverse phase; when $0^\circ < \theta < 180^\circ$, C_{Lrms} has a phase delay with Y.

Fig. 12 shows that the HISC has a phase difference between C_{Lrms} and Y when $U_r = 6$, and C_{Lrms} is in reverse phase with Y when $U_r > 7$. Combined with Fig. 11, the phase delay occurs when the vibration frequency f_Y is near the natural frequency f_n, then gradually increase with U_r. When C_L^{rms} is out of phase with Y, the vibration amplitude of HISC will weaken, and the amplitude will begin to decrease. For B2, when $d/D = 0.7$ and 0.8, ${C_{L2}}^{rms}$ and ${Y_2}^{max}$ are basically in reverse phase with the decrease of Y_2 at high U_r. When d/D increases to 1.2 and 1.4, the phase difference between ${C_{L2}}^{rms}$ and Y_2 decreases due to the high value of ${Y_2}^{max}$. However, with the sudden decrease of ${Y_2}^{max}$, ${C_{L2}}^{rms}$ is basically in the reverse phase with ${Y_2}^{max}$. For B3, since ${Y_3}^{max}$ is larger than ${Y_2}^{max}$ at corresponding d/D when U_r is high, ${C_{L3}}^{rms}$ and ${Y_3}^{max}$ are not in reverse phase, and in most cases, θ_3 is smaller than θ_2. It is also noticed in Fig. 12 that θ_2 and θ_3 vary simultaneously for different d/D. However, the phase change mechanism of θ_3 is more complex due to the strong nonlinearity of the thermal-fluid-structure coupling in the downstream region.

Fig. 13 shows a surface partition of the semi-circular cylinder to provide a clear understanding of the interpretations in the

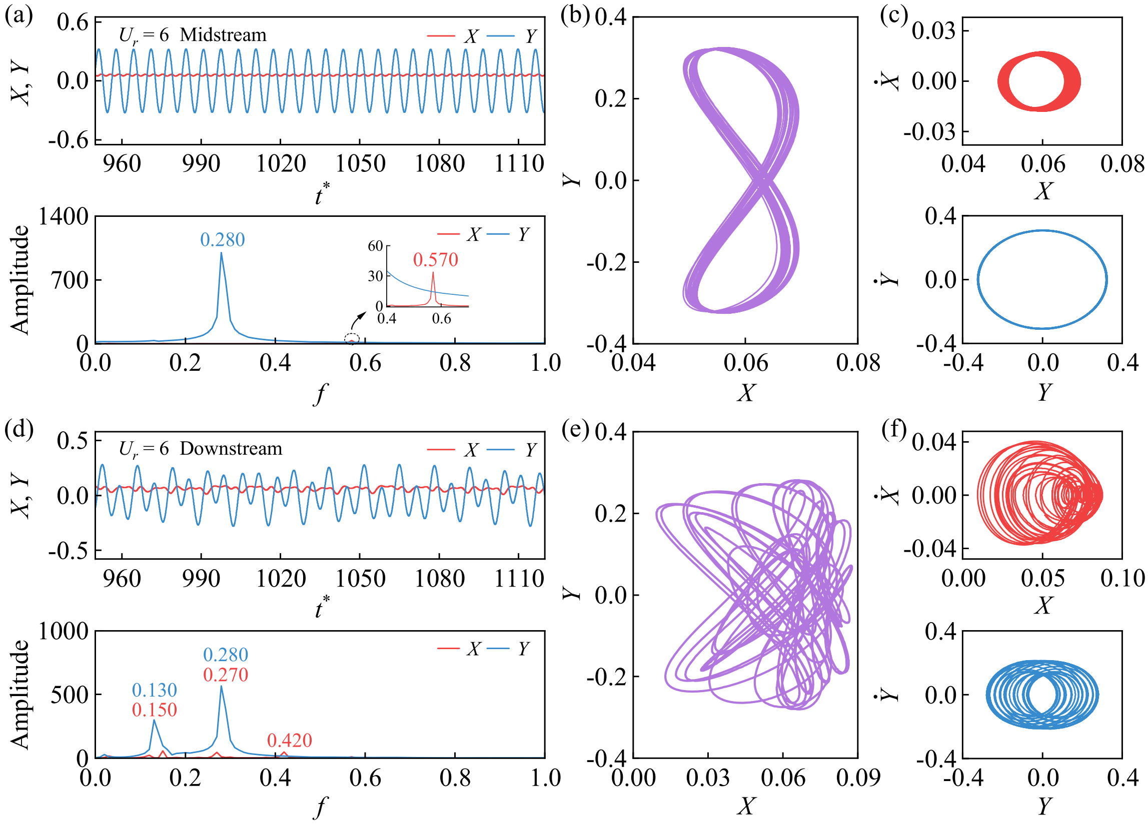

Fig. 16. The displacement time histories and the frequency contours, trajectories, and phase plots of the midstream (B2) and downstream (B3) bluff bodies at $U_r = 6$: (a)&(d) displacement time histories; (b)&(e) trajectories; (c)&(f) phase plots.

subsequent results. As shown in Fig. 13, the parameter φ is the rotation center angle of the bluff body. According to Barati *et al.* (Barati et al., 2022), the right side between the upper vertex and the lower vertex is the back surface, so the φ of the back surface ranges from 116°−244°, and the front surface ranges from 0°−53° and 307°−360°.

As shown in Fig. 14, the vibration behaviors of the HISC can be explained as a resonance phenomenon. When the vortex shedding frequency is close to the natural frequency, the large amplitude vibration will be excited over a range of U_r. With U_r further increases, the vibration amplitude of HISC decreases. However, the vibrations of the downstream cylinders are excited by their own vortices and also affected by the wake vortices of the upstream bluff body. The vibrations of the downstream cylinders are influenced by the following two major factors:

The first factor is wake instability. Unlike the uniform incoming flow of the HISC, B2, and B3 are submerged in a more unstable wake flow because the interference of the upstream cylinder significantly enhances the flow instability. These unstable flows exert an extra aerodynamic force on B2 and B3. This is one of the reasons why the vibration amplitudes of the downstream bluff bodies are much larger than that of the HISC at most U_r.

Another factor that affects the amplitude of the bluff body is the synergistic effect between the vibration of the downstream bluff body and the vortex shedding of the upstream bluff body. As shown in Fig. 14(a)&(c), when B2 reaches the uppermost position at instant $1^\#$, a negative vortex shed from B1 collides with the upper side surface of B2. Consequently, the downward motion of B2 is decelerated, resulting in a smaller amplitude at $U_r = 6$. In addition, the vortex generation of B3 is inhibited, and alternating vortices generated by B2 provoke the vibration of B3. Therefore, the vibration amplitude of B3 is lower than B2. In addition, the phase plots are presented to help characterize the dynamic responses (Rajamuni et al., 2020; Sareen et al., 2018). The transverse phase plots in Fig. 14(b) show that the motion of B2 and B3 is more periodic under the inhibition effect.

For the case of $U_r = 11$, as shown in Fig. 14(d)&(f), when B3 reaches the uppermost position at instant $1^\#$, the vortex shed from B2 just reaches the lower side surface of B3. Accordingly, the downward motion of B3 is accelerated, resulting in a higher amplitude at $U_r = 11$. Also, as shown in Fig. 14(e), the motion of B3 becomes chaotic. Then, at instant $2^\#$, when B2 reaches the lowermost position at instant $2^\#$, the vortices generated by B1 almost do not affect B2, and thus the vibration of B2 is nearly unaffected. However, at instant $1^\#$, it can be observed that when B2 moves to the lowermost position, a negative vortex street collides on the upper side surface of B2 and merges with the vortices generated by B2. Therefore, the vibration amplitude of B2 decreases at $U_r = 11$. Compared with B3, Fig. 14(e) shows that the motion of B2 is still periodic.

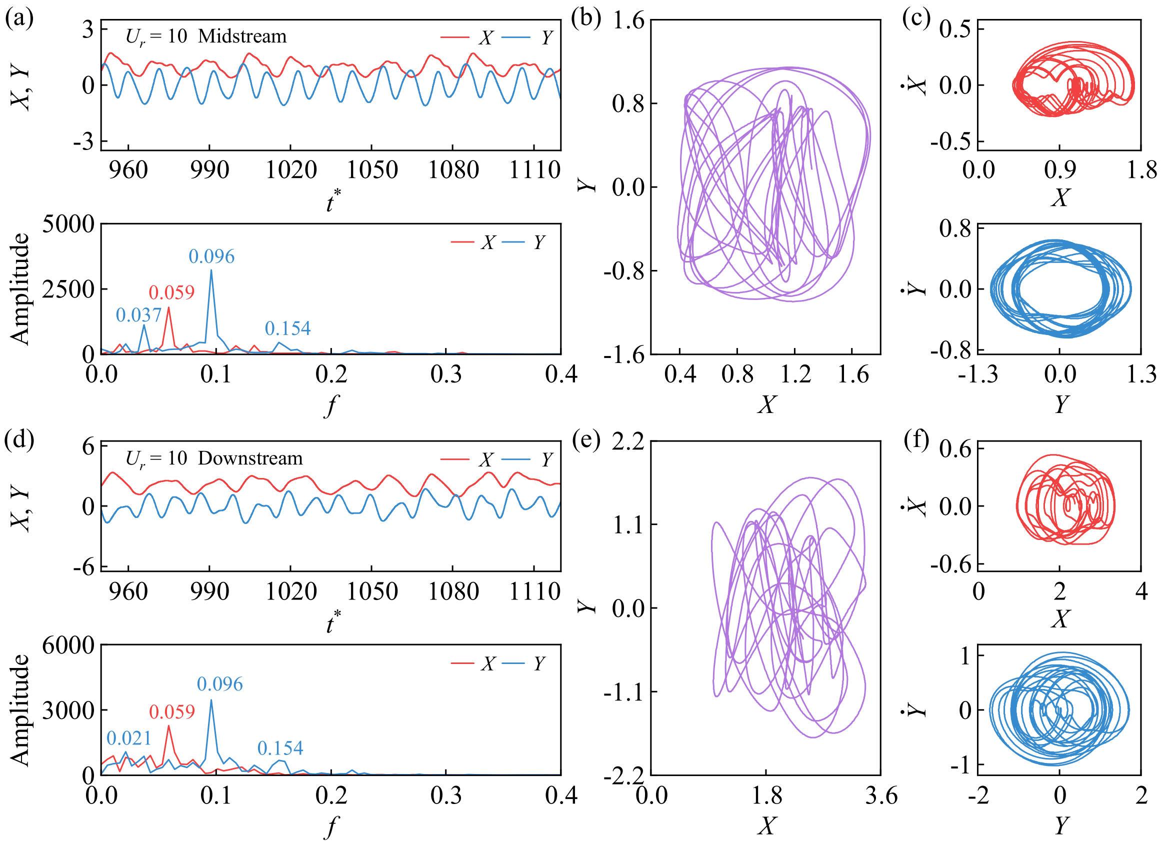

Fig. 17. The displacement time histories and the frequency contours, trajectories, and phase plots of the midstream (B2) and downstream (B3) bluff bodies at $U_r = 10$: (a)&(d) displacement time histories; (b)&(e) trajectories; (c)&(f) phase plots.

4.3. Trajectories and displacement responses

Bluff bodies often present various motion trajectories in multi-bluff body WIV problems. The study of the motion trajectory plays a vital role in controlling the multi-bluff body WIV. The service life of the equipment can be increased by suppressing the vibration, and the motion state of the fluid in the flow field can be changed by enhancing the vibration to improve certain effects of the equipment. To be concise, cases for B2 and B3 of $d/D = 1.4$ at $U_r = 2$, 6, 10, 14 are first studied to explore the dynamic responses. The trajectories, time-history displacement responses, phase plots and frequency contours are plotted in Figs. 15–18. The frequency contours are obtained by the FFT processing to explain the occurrence of different trajectories.

As shown in Fig. 15(a), the time-history displacement responses of B2 are relatively stable, and the vibration amplitude is quite small. The wake interference shows the QCS pattern at $U_r = 2$ between B1 and B2. The 2DOF vibration of B2 presents a typical thinner and taller ‘figure-eight’ shaped trajectory because the vibration frequency in the streamwise flow direction $f_X = 0.304$ is about twice that in the transverse flow direction $f_Y = 0.149$. The phase plots in Fig. 15(c) exhibit circular orbits, indicating a highly periodic dynamic response. Fig. 15(d) shows that B3 starts to become less stable, and the vibration amplitude is smaller than B2 in the two directions, and the dominant vibration frequency in the streamwise flow direction $f_X = 0.304$ is still about twice that in the transverse flow direction $f_Y = 0.149$, but the inter-harmonics causes the trajectory of B3 to show an unstable ‘figure-eight’ shape and the phase plots in Fig. 15(f) become a little disordered. The wake interference between B2 and B3 is the QCS pattern. From the perspective of nonlinear dynamics, the motions of the two bluff bodies are limit cycle oscillations (LCOs).

As shown in Fig. 16, the equilibrium position of the bluff body starts to move downstream at $U_r = 6$. The displacement responses of B2 at $U_r = 6$ are still stable, and the vibration amplitude in the x-direction is much smaller than the y-directional component. The wake interference between B1 and B2 still shows the QCS pattern. The trajectory of B2 presents a remarkably thinner and taller ‘figure-eight’ shaped trajectory compared with $U_r = 2$ because the vibration amplitude in the transverse flow direction is much larger than in the streamwise flow direction. The vibration frequency in the streamwise flow direction $f_X = 0.570$ is about twice that in the transverse flow direction $f_Y = 0.280$. The phase plots in Fig. 16(c) show circular orbits, and the motion of B2 is still limit-cycle oscillation (LCO). We can see from Fig. 16(d) that the displacement responses of B3 become irregular compared with B2. The vibration amplitude in the transverse flow direction is still much larger than that in the streamwise flow direction. The dominant vibration frequency in the streamwise flow direction $f_X = 0.270$ is almost equal to that in the transverse flow direction $f_Y = 0.280$. Therefore, the trajectory of B3 does not exhibit a ‘figure-eight’ shape, and the more inter-harmonics cause the trajectory of B3 to show an irregular shape. The wake

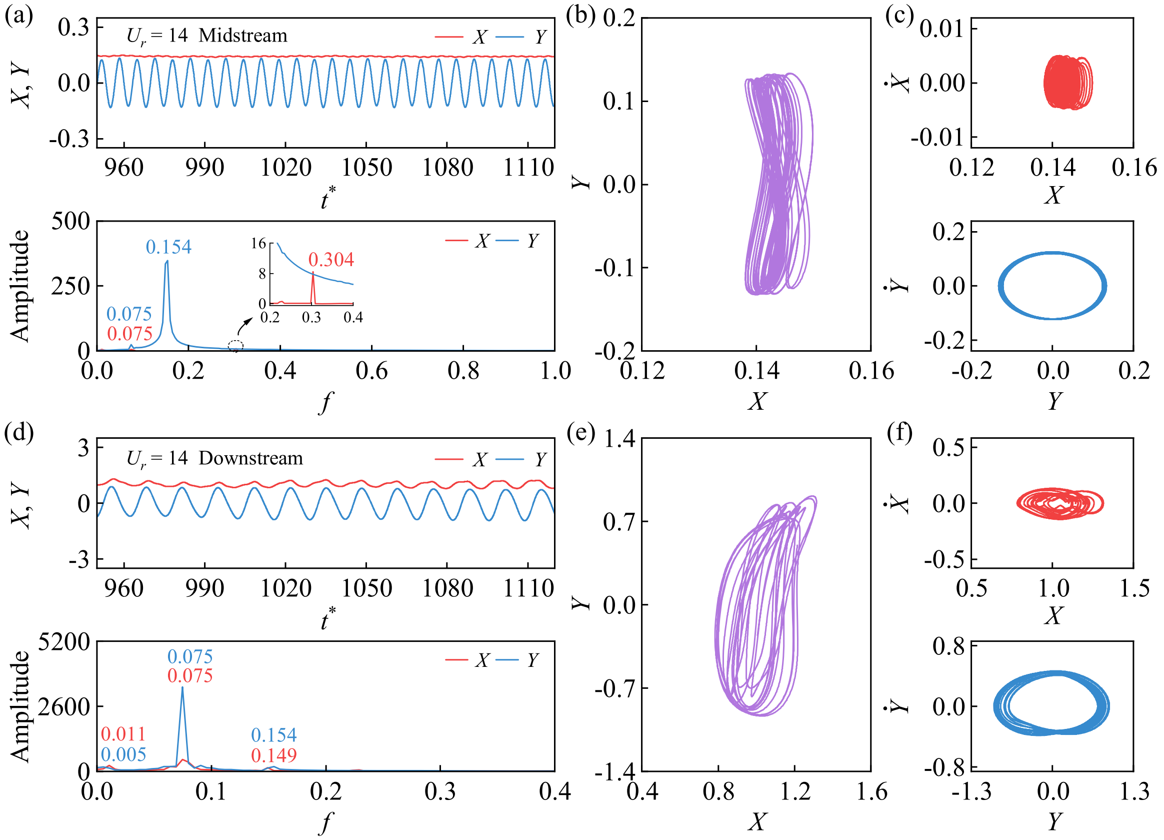

Fig. 18. The displacement time histories and the frequency contours, trajectories, and phase plots of the midstream (B2) and downstream (B3) bluff bodies at $U_r = 14$: (a)&(d) displacement time histories; (b)&(e) trajectories; (c)&(f) phase plots.

interference between B2 and B3 shows a QCS-CS pattern. The phase plots in Fig. 16(f) depict the chaotic motion of B3.

As shown in Fig. 17, the equilibrium position of the bluff body has evidently moved downstream at $U_r = 10$. The displacement responses of B2 and B3 become extremely unstable and contain many inter-harmonics. The wake interference pattern between B1 and B2 has changed to CS, and the trajectory of B2 presents a highly irregular shape. The dominant vibration frequency of B2 in the streamwise flow direction $f_X = 0.059$ is about 0.62 times that in the transverse flow direction $f_Y = 0.096$. According to the phase plots shown in Fig. 17(c), the motion of B2 at $U_r = 10$ becomes chaotic compared with B2 at $U_r = 2$ and 6. The motion of B2 has become chaotic compared with B2 at $U_r = 2$ and 6. Fig. 17(e) shows that the displacement response of B3 is still irregular, and there are many inter-harmonics. The wake interference between B2 and B3 exhibits the CS pattern. The dominant vibration frequency of B3 in the streamwise flow direction $f_X = 0.059$ is about 0.62 times that in the transverse flow direction f_Y =0.096. Fig. 17(f) shows the most highly nonlinearity and the motion of B3 becomes highly chaotic. In general, the above analysis indicates that the WIV of the bluff body exhibits strong nonlinearity in the 'lock-in' region.

Finally, Fig. 18 shows that the WIVs of the B2 and B3 re-enter stable states. The phase plots in Fig. 18(c)&(f) depict chaos in the x-direction and periodicity in the y-direction. In Fig. 18(a), the dominant frequency of the streamwise flow direction $f_X = 0.304$ is about twice that in the transverse flow direction $f_Y = 0.154$, which also leads to the typical 'figure-eight' shape in the trajectory of B2. The wake interference pattern between B1 and B2 has changed to QCS, and the vibration becomes a relatively stable LCO. The vibration of B3 also becomes stable. The trajectory shape of B3 is circular because the dominant frequency f_X is the same as f_Y, but the trajectory shows weak chaos due to some weak harmonics. The wake interference pattern between B2 and B3 shows QCS-CS due to the large vibration amplitude of B3. It also shows that the nonlinearity of the WIV in our case with multiple bluff bodies is stronger than that in a single bluff body, and the vibration regularity is also more complex.

4.4. Aerodynamic response and Nusselt number

In addition to the lift force coefficient C_L^{rms}, the drag force coefficient C_D is another important parameter for evaluating the nonlinear dynamics and heat transfer of the bluff bodies. The time-averaged drag force coefficient C_D^{mean} can be calculated as:

$$C_D^{mean} = \frac{1}{N} \sum_{i=1}^{N} \frac{2F_D^i}{\rho U_\infty^2 D} \tag{32}$$

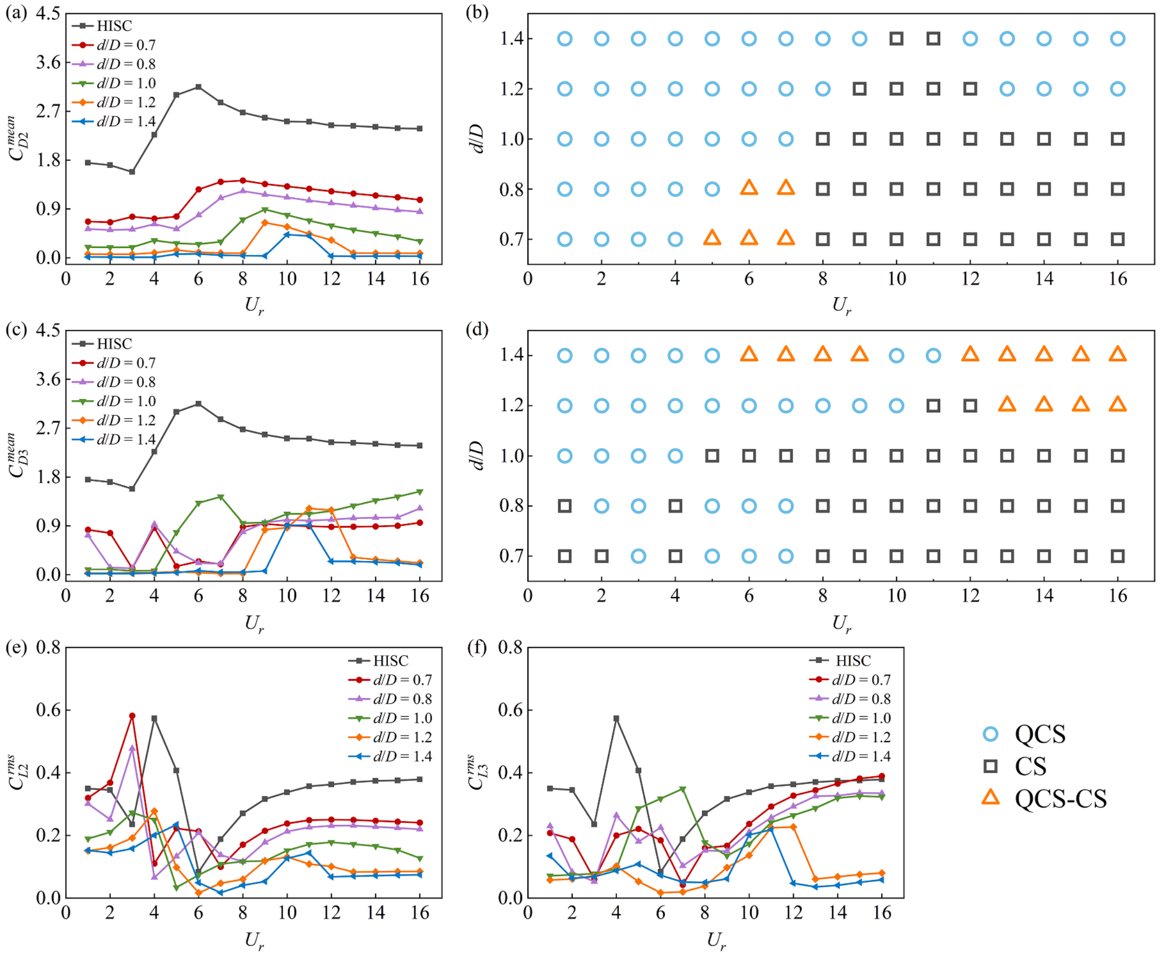

Fig. 19. Variation of C_D^{mean} and C_L^{rms} with the reduced velocity for different bluff bodies: (a)&(e) B2; (c)&(f) B3. Subfigures (b)&(d) are the wake interference patterns to give a clear comparison with C_D^{mean} and C_L^{rms}.

where F_D^i is the drag force and i starts from a stable vibration period. Fig. 20 compares C_D^{mean} and C_L^{rms} of B2 and B3 against the HISC.

For the VIV of the HISC, C_D^{mean} increases over the range of $U_r = 1$–4 at the initial branch (IB), as shown in Fig. 19(a). Then, C_D^{mean} decreases over $U_r = 5$–7 at the lower branch (LB). C_D^{mean} stays stable within the range of $U_r = 8$–16, which is the desynchronization branch (DB). For the other d/D, ${C_{D2}}^{mean}$ decreases as d/D increases because the front of B2 is obstructed more by B1. The variation trend of ${C_{D2}}^{mean}$ is similar to that of the HISC, especially when $d/D = 0.7$ and 0.8, because the vibration characteristics of B2 are more consistent with HISC. The similarity begins to weaken from $d/D = 1.2$, and with the increase of the diameter of B1, ${C_{D2}}^{mean}$ continues to decrease. For $d/D = 1.4$, due to the complete blocking effect of B1, ${C_{D2}}^{mean}$ approaches to zero in QCS pattern. As shown in Fig. 19(c), for the other d/D, since the vortex street has been completely developed after passing through B1 and B2, ${C_{D3}}^{mean}$ remains at a low level and only increases over the CS pattern region. Once the wake interference shows characteristics of the QCS pattern, ${C_{D3}}^{mean}$ begins to decrease significantly.

As shown in Fig. 20(a), for $d/D = 1.2$, B2 suffers an unstable C_D fluctuation when $U_r = 10$. Considering that in CS mode, the evolved vortex completely sheds from B1 and reattaches to the surface of B2 after a period of time (Fig. 20(b)). In general, the vortex center velocity is faster than the vortex periphery velocity, leading to a lower pressure in the vortex center. Accordingly, at $U_r = 10$, the vortex shed from B1 could lead to a large C_p variation on the surface of B2, and the C_p difference between the front and back surfaces of B2 contributes to a C_D fluctuation. In the QCS pattern, the evolved vortex from B1 flows around B2 and results in a stable C_p and an inconspicuous C_D fluctuation on the surface of B2.

Because of the symmetry, time-averaged C_p^{mean} distributions on the lower half of HISC and B2 are discussed. We can see from Fig. 21 that the maximum C_p^{mean} occurs at the front stagnation point ($\varphi = 0°$), the flow separates from the sharp edge ($\varphi = 116°$, C_p^{mean} drops dramatically and shows a highly negative value), then C_p^{mean} keeps a relatively constant value on the back surface ($116° < \varphi < 180°$). The large C_p^{mean} variation between the front and back surfaces of the semi-circular bluff body determined a monotonic increase of X^{mean} with U_r. For $d/D = 0.7$, due to the "blocking effect" of B1, the C_p difference between the front and back surfaces of B2 decreases, resulting in a slower growth of ${X_2}^{mean}$ and for $d/D = 1.2$. C_p^{mean} of B2 shows a large variation in CS pattern, indicating that ${X_2}^{mean}$ only

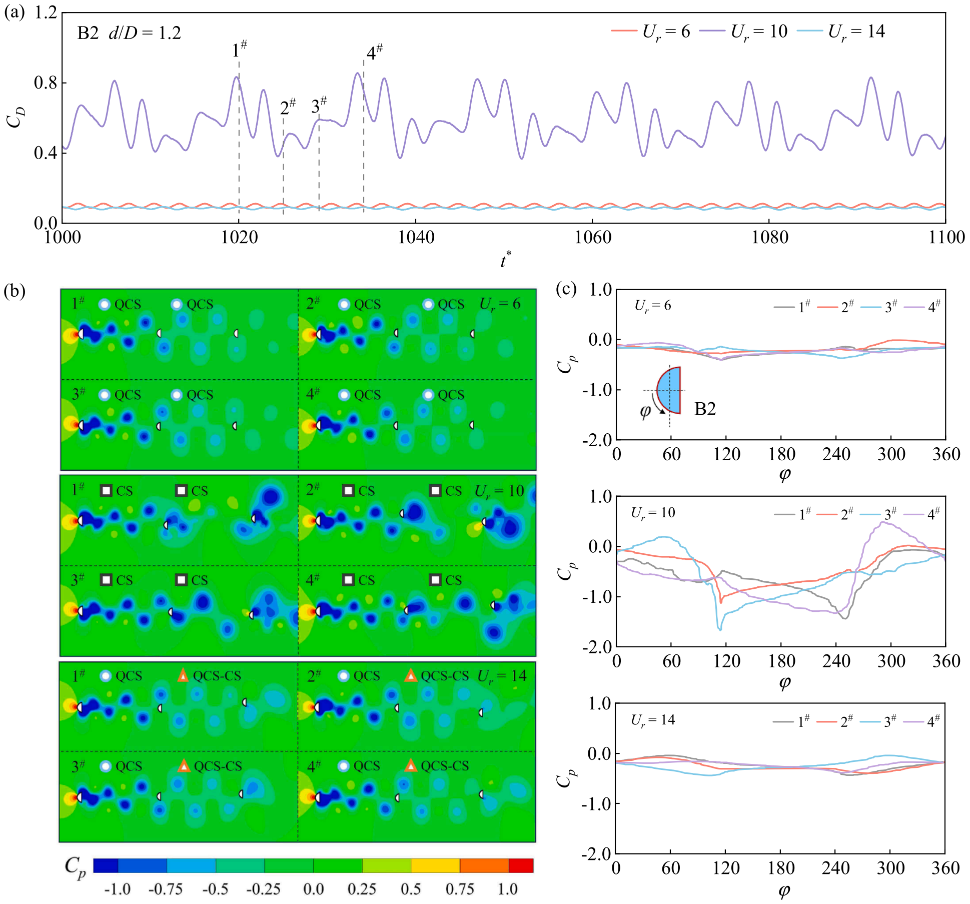

Fig. 20. (a) the C_D time histories of B2 at $d/D = 1.2$, $U_r = 6, 10, 14$; (b) pressure coefficient C_p contours at different instants; (c) the local C_p around B2 with different U_r at the corresponding instant.

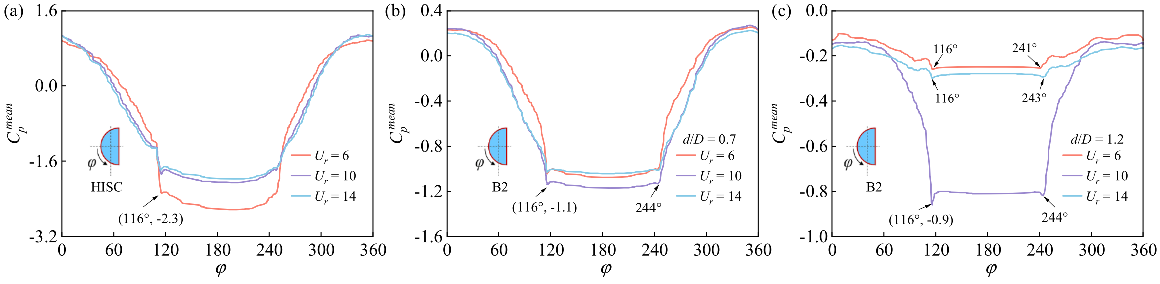

Fig. 21. The time-averaged C_p^{mean} around the HISC and B2 ($d/D = 1.2$) at $U_r = 6, 10, 14$: (a) HISC; (b) B2 at $d/D = 1.2$.

increases when B2 shows a large transverse amplitude at $U_r = 9$–12, and the same conclusions also apply for B3.

Unlike C_D^{mean}, the RMS amplitude of the lift coefficient of the HISC C_L^{rms} first decreases and then increases over the IB region ($U_r = 1$–4). It keeps decreasing over the LB region ($U_r = 5$–7). After that, it slowly increases and stabilizes in the DB region ($U_r = 8$–16). For B2, ${C_{L2}}^{rms}$ in the entire U_r range is similar to the HISC for $d/D = 0.7$ and 0.8. As d/D increases, ${C_{L2}}^{rms}$ gradually decreases, which is probably related to the diameter ratio d/D and the wake interference pattern. For B3, ${C_{L3}}^{rms}$ decreases again, and the lift coefficients for all d/D are not very large at most U_r. It can be seen that the fluctuation of ${C_{L3}}^{rms}$ is relatively stable due to the 'blocking effect' of B1 and B2.

Fig. 22(a) and Fig. 22(c) show the variation of Nu_A for B2 and B3. For B2, the distribution of Nu_{A2} is similar to ${C_{D2}}^{mean}$, showing a more relaxed state. Nu_{A2} decreases with the increase of d/D but increases with the increase of ${Y_2}^{max}$ because a large vibration amplitude of B2 weakens the blocking effect of the upstream bluff bodies. The probability for B2 to face the incoming fluid increases. In the five groups of d/D, the maximum $Nu_{A2} = 7.08$ occurs at $d/D = 0.7$ and $U_r = 8$, which is 19.55% smaller than the HISC ($Nu_A = 8.80$)

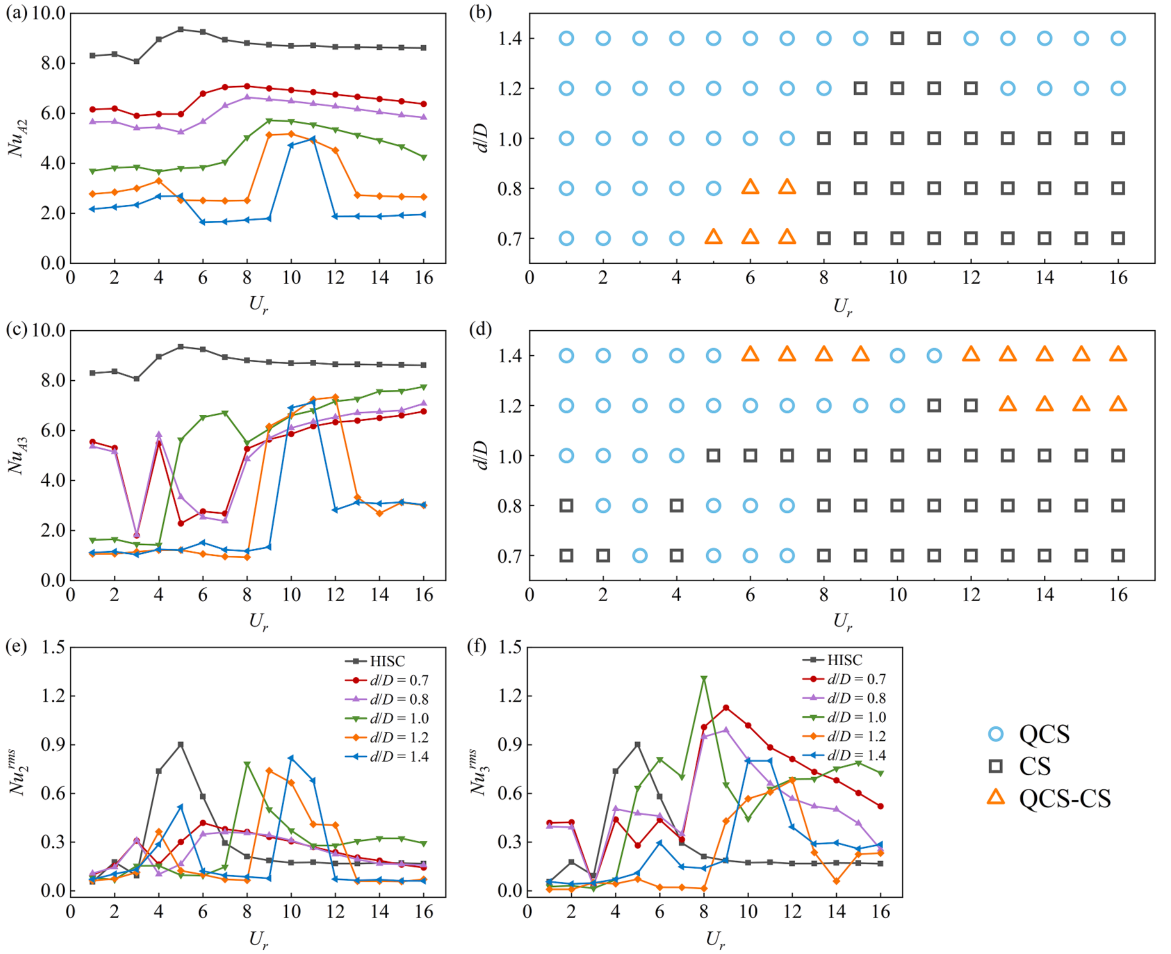

Fig. 22. Variation of Nu_A and Nu^{rms} with the reduced velocity for different bluff bodies: (a)&(e) B2; (c)&(f) B3. Where (b)&(d) are the wake interference patterns so as to give a clear comparison with Nu_A and Nu^{rms}.

under the same conditions.

For B3, the only difference from B2 is that the variation of Nu_{A3} shows a more compact state but is still similar to $C_{D3}{}^{mean}$. Nu_{A3} does not decrease dramatically with the ‘blocking effects’ of B1 and B2, but sometimes shows a larger value than B2 due to the large vibration amplitude in the lock-in regions. For instance, at $d/D = 1.0$ and $U_r = 12$, Nu_{A3} is 7.17 and 34.02% higher than $Nu_{A2} = 5.35$ under the same conditions.

Similar to C_L^{rms}, the RMS amplitude of the time-averaged Nusselt number Nu^{rms} represents the deviation from Nu_A. It can be calculated by the following equation:

$$Nu^{rms} = \sqrt{\frac{1}{N}\sum_{i=1}^{N}\left(Nu_S^i - Nu_A\right)^2} \tag{33}$$

where Nu_S^i is the surface-averaged Nusselt number at the instant i. As shown in Fig. 22(e)-(f), for the VIV of the HISC, Nu^{rms} increases within $U_r = 1$–4, then decreases over $U_r = 5$–7, and finally stays stable for $U_r = 8$–16. For the other d/D, it is easy to see that the variation of Nu^{rms} is consistent with the changes of transverse amplitudes in Fig. 11 and Fig. 22. Especially in the ‘lock-in’ region, the higher the amplitude, the more obvious the variation of Nu^{rms}. This is because the higher amplitude of the bluff body disturbs the vortex-shedding process, thus strengthening the convective heat transfer of B2 and B3.

The effect of U_r on the dimensionless vibration amplitude and the Nu are shown in Fig. 23. The Nu_A and Nu^{rms} for the flow around fixed tandem semi-circular at $d/D = 0.7$ are also presented for comparison. It can be noted that the variation trend of Nu^{rms} is similar to the corresponding transverse amplitude over $U_r = 1$–16. For B2, the transverse amplitude is much larger than the streamwise amplitude. For B3, we can see that the streamwise amplitude is larger than the streamwise amplitude after $U_r = 10$. That is due to the following reason: a smaller d/D leads to a smaller velocity change and a narrow vortex street width then contributes to weaker vortices from B1 and stronger vortices behind B2; B3 suffers an intense and unstable high-frequency vortex impact from B2 in the CS pattern,

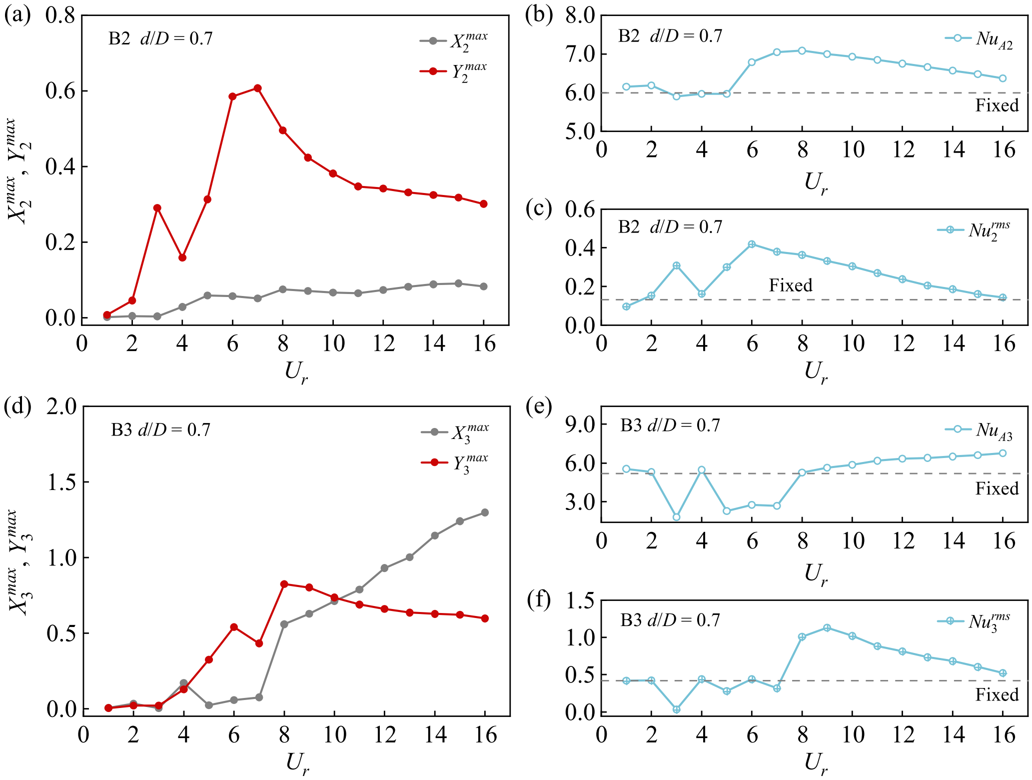

Fig. 23. The variation of dimensionless vibration amplitudes and Nu_A, Nu^{rms} of B2 and B3 with U_r at $d/D = 0.7$: (a)-(c) B2; (d)-(f) B3.

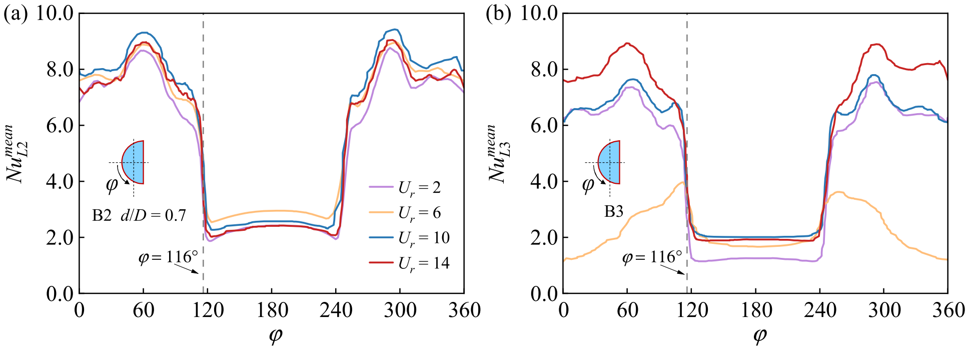

Fig. 24. Time-averaged Nu_L distributions around the surface of B2 and B3 for different U_r at $d/D = 0.7$: (a) B2; (b) B3.

leading to a monotonous increase of X_3^{rms} after $U_r = 7$. However, it can be seen in Fig. 11 that this phenomenon gradually diminishes with the increases of d/D. In addition, it can be seen that Nu_3^{rms} is higher than Nu_2^{rms}, owing to the high vibration amplitude of B3, and the vortices shed off from B2 carry an amount of thermal energy.

As shown in Fig. 24, the lower half of B2 and B3 are discussed. Different from C_p, the maximum Nu_L^{mean} is not obtained at the front stagnation point ($\varphi = 0°$), and the minimum Nu_L^{mean} is also not obtained at the rear stagnation point ($\varphi = 180°$). However, we can observe that Nu_L^{mean} rapidly drops near $\varphi = 116°$, which is caused by the flow separation. At the separation point, the boundary layer separates, the thermal resistance increases, and the heat transfer decreases. Increasing Nu_L on the left surface of the flow separation point is vital in enhancing heat transfer because the left surface of the midstream and downstream bluff body is affected by unstable vortices and thus presents different Nu.

We can assume that the changes in the temperature boundary layer and velocity boundary layer follow a similar trend at low Re. For flow around bluff bodies, the velocity gradients within the boundary layer gradually decrease in the flow direction until they reach zero at the boundary layer separation point (H.J. Zhu et al., 2020). In the convective heat transfer of FIV, the heat transfer is achieved through a combination of convection and diffusion. Convection is dependent on the magnitude of velocity gradients. Therefore, a decrease in velocity gradients results in a decrease of Nu_L on the surface convection. On the other hand, diffusion is not affected by the

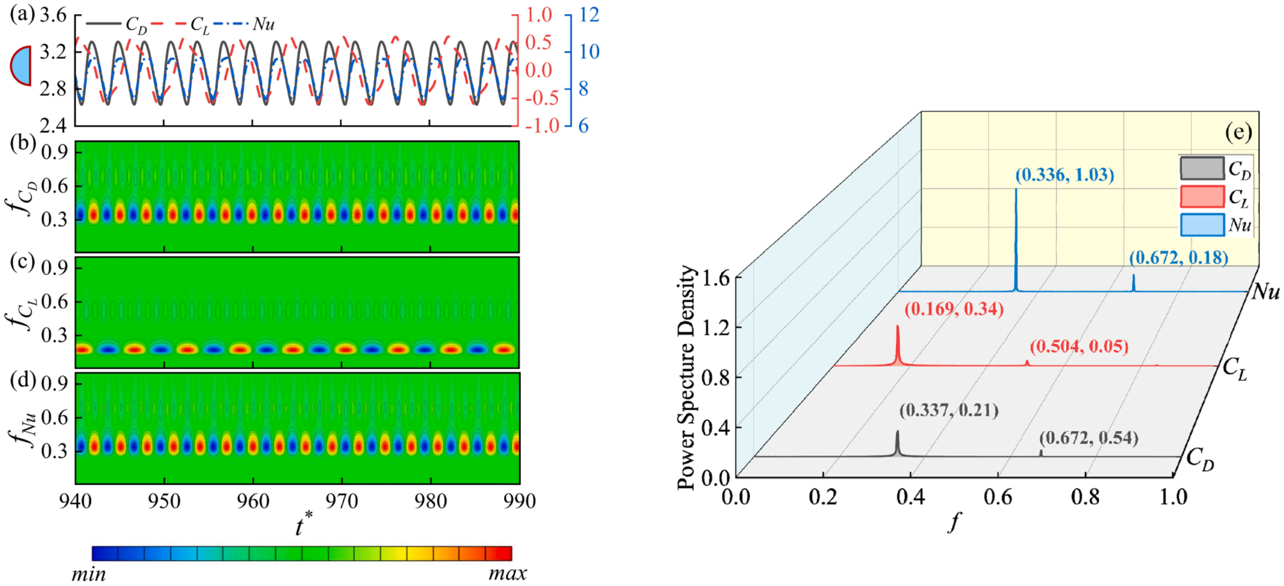

Fig. 25. Time histories (a) of C_D, C_L, Nu, and CWT contours (real part) of (b) C_D, (c) C_L, (d) Nu and the FFT spectrum (e) of C_D, C_L, Nu for the HISC.

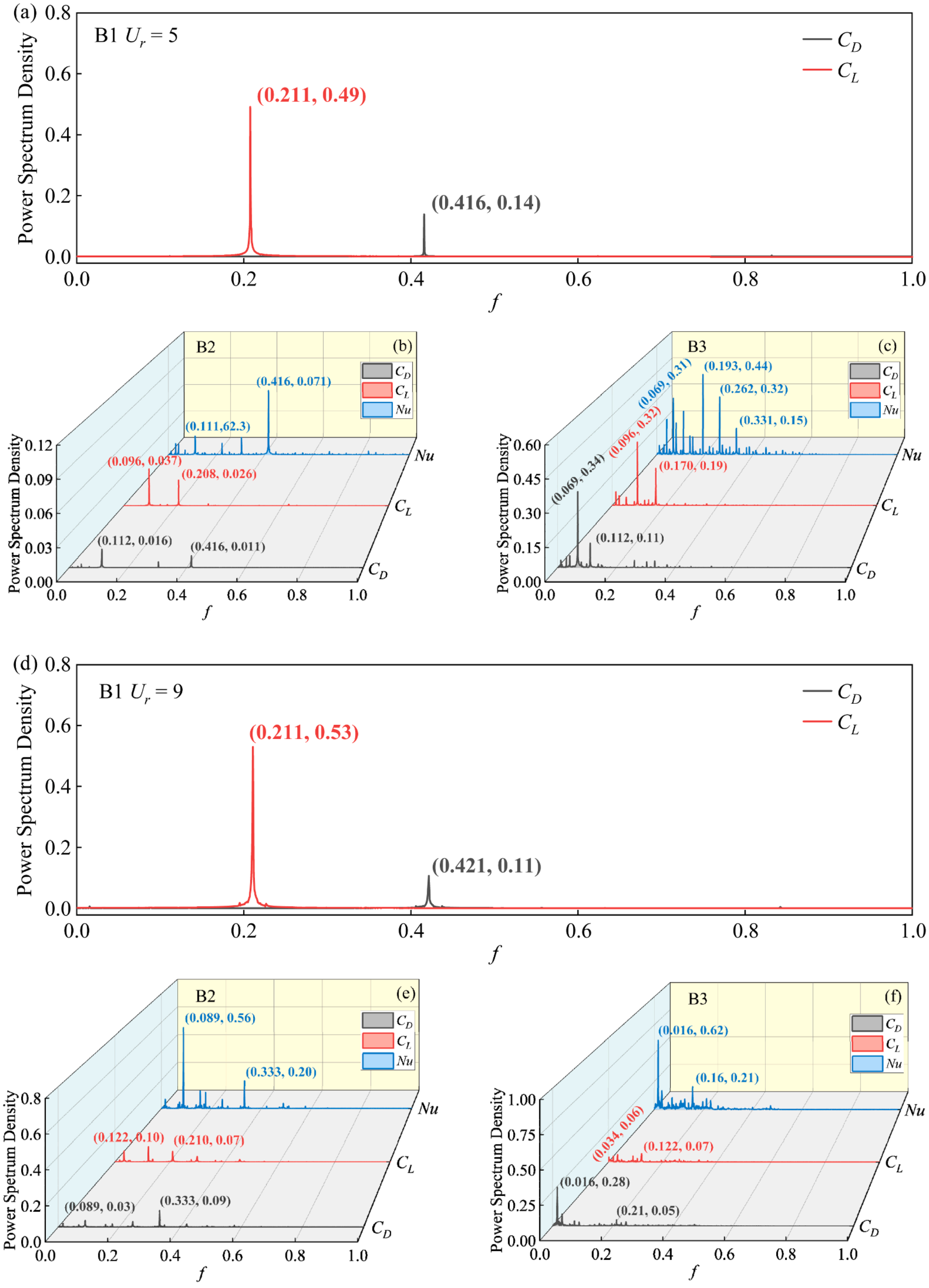

Fig. 26. Fast Fourier transform of C_D, C_L, Nu time histories for $d/D = 1.0$ and $U_r = 5$, 9: (a)-(c) $U_r = 5$; (d)-(e) $U_r = 9$.

velocity. Consequently, the overall heat transfer varies with the change of boundary layer velocity gradient, and Nu_L^{mean} sharply decreases near $\varphi = 116°$. For B3 at $U_r = 6$, the Nu_L^{mean} first increases before $\varphi = 116°$, and then sharply decreases. The reason for the increase is that the vortices only pass through the upper and lower sides of the bluff body in the QCS pattern, resulting in a higher velocity gradient on those sides.

The relationship between Nu, C_D, and C_L can be illustrated by fast Fourier transform (FFT) and continuous wavelet transform (CWT). Two complex-valued (Gabor and Bump) wavelets are generally employed in practice. The Gabor wavelet provides a narrow variance in frequency resolution and a wide variance in time resolution. The Bump wavelet provides a narrower variance in time

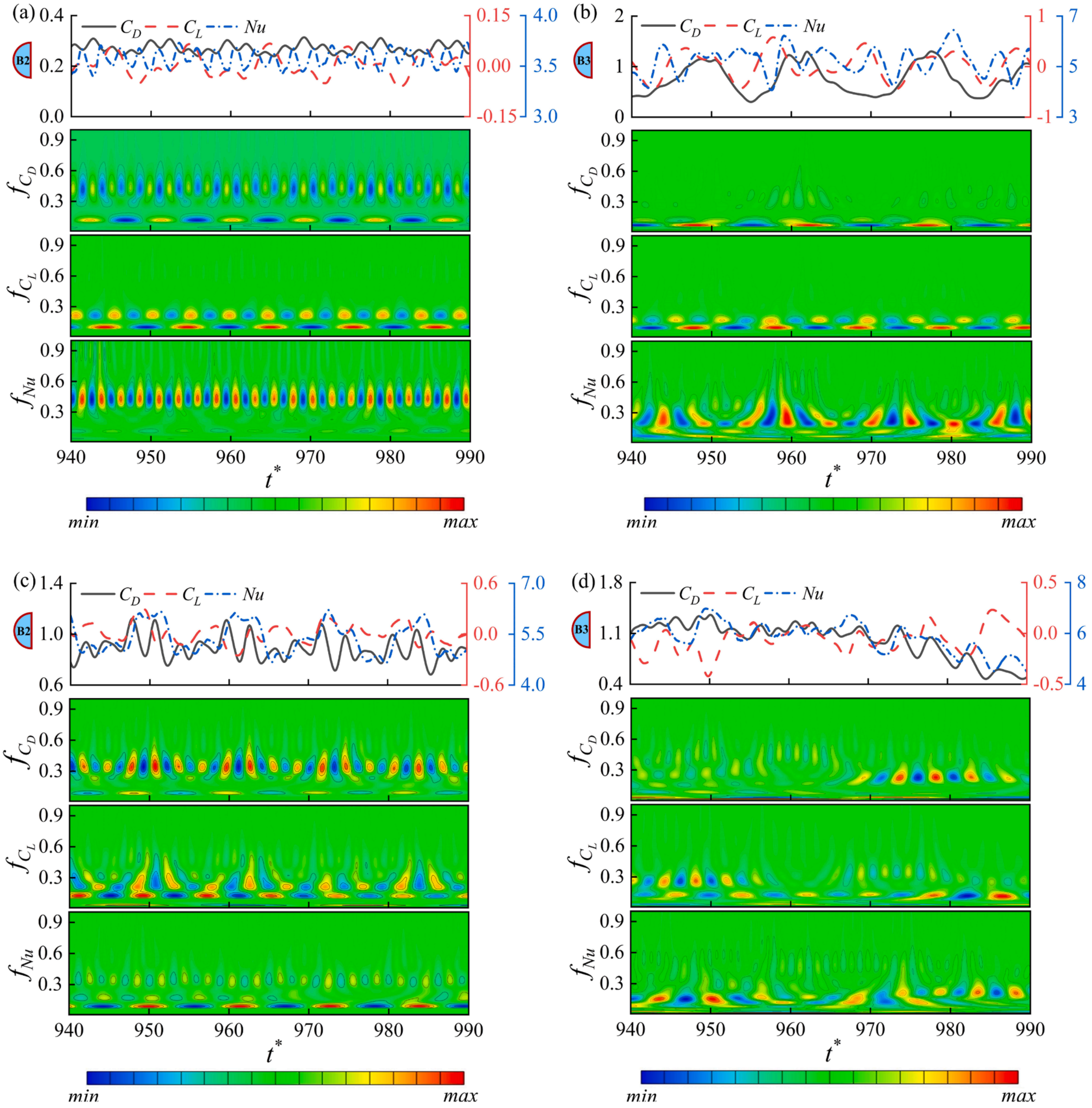

Fig. 27. Time histories of C_D, C_L, Nu and its wavelet contours (real part) of B2 and B3 at $d/D = 1.0$ and $U_r = 5, 9$: (a)&(b) B2 and B3 at $U_r = 5$; (c)& (d) B2 and B3 at $U_r = 9$.

resolution but a wider variance in frequency resolution compared with the Gabor wavelet. According to the characteristics of the signal and its intrinsic connection, the Gabor wavelet is chosen to plot the real part of the continuous wavelet analysis results and trace the minima and maxima of a signal (Hamdan et al., 1996). The wavelet contour and FFT spectrum of C_D, C_L, and Nu time histories for the HISC at $U_r = 5$ is shown in Fig. 25. In the wavelet contour and FFT spectrum results of C_D, i.e., Fig. 25(b) and Fig. 25(e), the wavelet contour basically shows a single frequency fluctuation and the alternating peaks and roots mostly appearing at $f_{C_D} = 0.337$ represent the maximum and minimum values of C_D [Fig. 25(a) and Fig. 25(e)]. Similarly, the wavelet contour of C_L and Nu also shows a single frequency fluctuation. The alternating peaks and roots of C_L and Nu mostly appear at $f_{C_L} = 0.169$ and $f_{Nu} = 0.337$, respectively. It can be found that $f_{C_D} \approx f_{Nu} \approx 2f_{C_L}$, the time-domain results and the wavelet contours of C_D and Nu are similar, indicating that the heat convection of the HISC is primarily driven by the drag force.

To avoid redundancy, the time histories of C_D, C_L, and Nu, the FFT and CWT results for B2 and B3 at the case of $d/D = 1.0$, $U_r = 5, 9$, and $t^* = 940$–990. are shown in Fig. 26 and Fig. 27, the FFT result of B1 is also presented to give a clear frequency comparison between C_D, C_L, and Nu of three bluff bodies. For B1 at $U_r = 5$, as shown in Fig. 26(a), the dominant frequencies f^d of C_D and C_L are 0.416 and 0.211. We can find in Fig. 26(a)-(b) that some aerodynamic frequency components of B2 are similar to B1 because B1 dominates the aerodynamic behavior of B2 in the QCS pattern. However, for B3 in Fig. 26(c) and Fig. 27(b) at CS pattern, the CWT and FFT results show that the aerodynamics of B3 exhibit multi-frequency characteristics, and the corresponding frequency components are generally

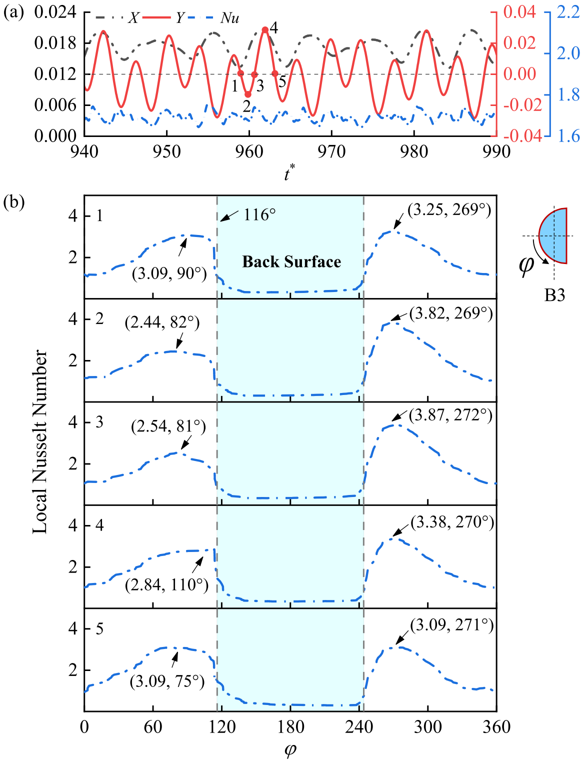

Fig. 28. Variation of local Nusselt number at QCS pattern for $d/D = 0.7$, $U_r = 3$: (a) five sampling points in a quasi-period; (b) variation of local Nusselt number.

different from those of B1 and B2, but we can still observe that $f^{d}_{C_L} = 0.096$ for B2 and B3 in Fig. 26(b)-(c). It should be noted for B2 and B3 in Fig. 26(b)-(c) that some frequency components between C_D and Nu are the same. For example, $f^{sec}_{C_D} = f^{d}_{Nu} = 0.416$ in Fig. 26(b). Similar results are also observed for B3 at $U_r = 9$ in Fig. 27(e)-(f), such as: $f^{d}_{C_D} = f^{d}_{Nu} = 0.016$ in Fig. 26(f), indicating a certain correlation between Nu and C_D for midstream and downstream bluff body in QCS and CS patterns, although it is not evident in the CWT contours (Fig. 27). For C_L and Nu in the CS mode, some vortices shed off from the upstream bluff body will collide with the downstream bluff body surfaces, introducing cold air into the thermal boundary layer and causing frequency fluctuations of Nu for the downstream bluff body. Consequently, Nu of the downstream bluff body will be influenced by C_L and result in multi-frequency components. It is also the reason for the unstable variation of the aerodynamic frequency of the downstream bluff body over time, as shown in Fig. 27(b)-(d).

The Nu changes in one cycle of B3 in different patterns are analyzed to show the distribution of Nu. We choose B3 at $d/D = 0.7$ as an example because it is the most affected by the vortices from B1 and B2. As shown in Fig. 28(b) and Fig. 29, in the QCS pattern, because of the little ${Y_3}^{max}$ and the stable vortex shedding period, the Nu_L distributions of B3 at different instants are roughly similar. The minimum Nu_L areas are observed at the back zone at all five instants, that is owing to the following reason: the ‘blocking effect’ of B2 and the stable vortex shedding process in the QCS pattern cause the fluid in front of B3 to be almost stationary, resulting in the back zone of B2 has little vortices and a higher fluid temperature in front of B3; then the thermal boundary layer becomes thicker, and the heat transfer decreases, which decreases the local heat transfer. Two peak values of Nu_L are also observed about $\varphi = 81^\circ - 110^\circ$ and $\varphi = 269^\circ - 272^\circ$ at two side surfaces. Due to the partial vortices, the thermal boundary layer becomes thinner, and the thermal resistance is the lowest, which is conducive to forced convection.

As shown in Fig. 30 and Fig. 31, the Nu distributions of B3 at different instants are pretty different in the CS pattern. The large amplitude of ${Y_3}^{max}$ induces complex interaction of vortices, and B3 does not usually locate behind B2. Hence, the ‘blocking effect’ weakens, and the isotherm in front of B3 is denser, resulting in a higher Nu_L. Fig. 30 shows that the thermal boundary layers in back zones ($\varphi = 116^\circ - 244^\circ$) are still thick, and the Nu_L is still small but larger than $d/D = 0.7$, $U_r = 3$. Two peaks of Nu_L can be observed on two side surfaces and the front surface in a large range of $\varphi = 0^\circ - 114^\circ$ and $263^\circ - 347^\circ$ at five instants. Dense isotherms appear with a higher temperature gradient, resulting in a high Nu_L. Generally, B3 at instants 1 and 5 should have a similar temperature distribution because the ${Y_3}^{max}$ is quasi-zero, and B3 tends to move down. However, the difference in Nu_L distribution between instants 1 and 5 is that B3 may be affected by the vortices of B1 and B2, resulting in partial changes of Nu_L on its surface, but the trend is roughly consistent. B3 at instants 2 and 4 exhibits different temperature distributions because B3 reaches the local maximum, and the motion direction of B3 is opposite at the next moment. Therefore, we can conclude that the heat convection intensity is higher in the CS pattern, which helps enhance heat transfer. However, the higher amplitude ${Y_3}^{max}$ generally affects the service lifespan of the equipment.

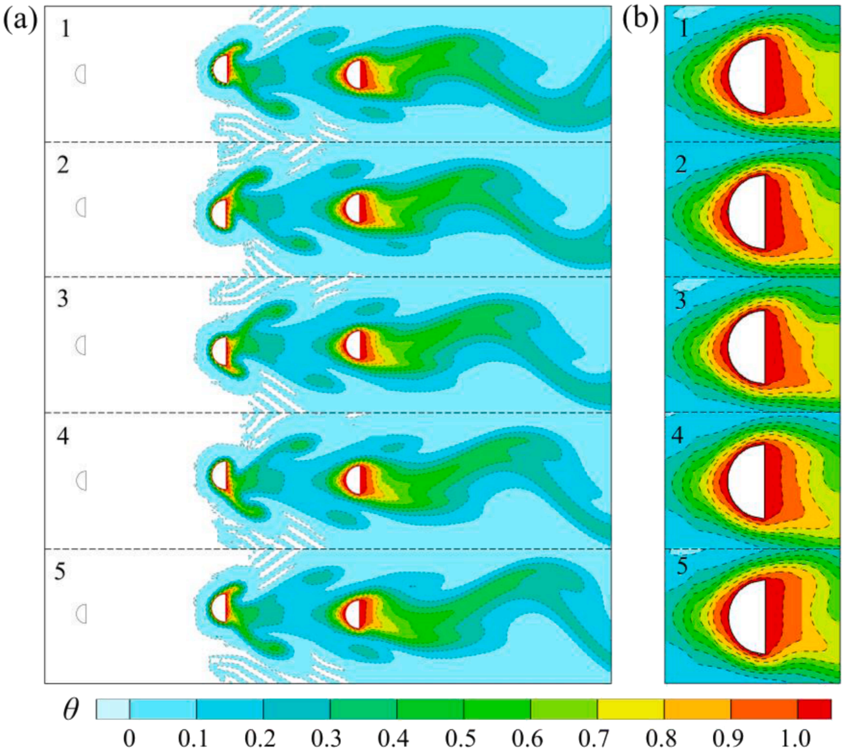

Fig. 29. Corresponding normalized temperature contours at five instants for $d/D = 0.7$, $U_r = 3$: (a) the global normalized temperature contours; (b) the local normalized temperature contours of B3.

At last, Fig. 32 shows the Nu_A increase rate under different d/D. Compared to the fixed conditions, at $d/D = 1.2$ and 1.4, the maximum increase of Nu_{A2} exceeds 67.7% in $U_r = 10$–11, but it is accompanied by a larger vibration amplitude. Furthermore, a significant decrease of Nu_{A2} is observed in $U_r = 6$–9 and 12–14 at $d/D = 1.4$, indicating that this operating condition should be avoided. However, there are still some instants that Nu_A shows a moderate increase at specific U_r. For B3, apart from the decrease in Nu_A in some QCS patterns, improvements are observed in other d/D. Notably, the improvement of Nu_{A3} exceeds 300% in some situations at $d/D = 1.2$ and 1.4. Nevertheless, it is essential to consider this situation cautiously due to the relatively low Nu_{A3} under fixed conditions and the decrease of Nu_{A2} at $d/D = 1.4$. For $d/D = 0.7$ and 0.8, except for some situations where Nu_A decreases or keeps almost unchanged at specific U_r, a certain degree of improvement in Nu_A is observed at the remaining U_r. Additionally, Nu_{A2} and Nu_{A3} are higher under fixed conditions, as shown in Fig. 32(a). Consequently, $d/D = 0.7$ and 0.8 are considered appropriate spacing ratios, obvious improvements of Nu_{A2} over 12% in $U_r = 7$–12, and a growing trend of Nu_{A3} are observed in $U_r = 9$–16.

5. Conclusions

In this paper, we have studied the wake-induced vibration and forced convection of two tandem bluff bodies under the influence of an upstream bluff body. The wake interferences between the bluff bodies have been classified into three patterns: CS, QCS, and QCS-CS. The midstream bluff body prohibits an intense but intermittent WIV in the streamwise and transverse directions, and the downstream bluff body has a large vibration amplitude in the streamwise direction and conducts an intensive WIV in the transverse direction under the influence of the midstream and upstream bluff bodies, Nu_A also shows improvement with the increase of transverse amplitude. The synergistic effect between the vortices of the three bluff bodies contributes to different vibration amplitudes, and the narrow vortex street of the upstream bluff body and the high vibration amplitude of the midstream and downstream bluff bodies are the significant reasons for the change of the wake interference from the QCS to the CS pattern. In addition, the phase delay (θ) between the lift force and transverse displacement indicates that the capability of the bluff body to absorb the kinetic energy of the fluid begins to weaken and serves as a good figure of merit to indicate the kinetic energy transfer state between fluid and vibrating structures. Through the time-history analysis, it is found that the trajectories of the midstream and downstream bluff bodies are often in the 'figure-eight' shape at low U_r, exhibiting limit cycle oscillations (LCOs). Then with the increase of U_r, the LCO begins to weaken and become chaotic. As U_r continues to increase, the trajectory of the bluff body is manifested as steady LCO again.

The aerodynamic response analysis has revealed that the time-averaged drag force coefficient C_D^{mean} and the time-averaged lift force coefficient C_L^{rms} of the midstream bluff body decrease with the increase of d/D because the upstream bluff body tends to block the incoming flow. C_D^{mean} and C_L^{rms} of the downstream bluff body often stay at low states in QCS patterns and only start to increase when the vibration amplitude of the downstream bluff body becomes relatively higher at specific U_r in the CS pattern. The time-averaged

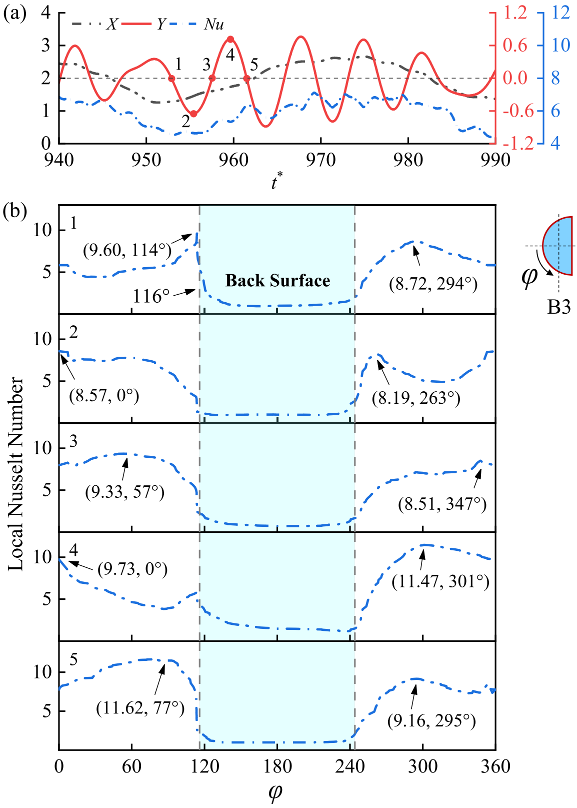

Fig. 30. Variation of local Nusselt number at CS pattern for $d/D = 0.7$, $U_r = 12$: (a) five sampling points in a quasi-period; (b) variation of local Nusselt number.

pressure coefficient C_p^{mean} on the surface of the midstream and downstream bluff body shows that the flow separation point is fixed at two vertices, that is, 116°.

In the CS pattern, the Nu_A of the midstream and downstream is generally higher than in the QCS pattern because the high transverse amplitudes of the midstream and downstream bluff bodies make the flow field more chaotic. Hence, the increase of transverse amplitude positively contributes to the convective heat transfer. The analysis of the surface time-averaged local Nusselt number Nu_L^{mean} indicates that increasing Nu_L on the front and side surfaces of the bluff body is a pivotal measure to enhance heat transfer.

The influences of the aerodynamic responses of the midstream and downstream bluff bodies on the Nusselt number (Nu) have been revealed by CWT and FFT analyses. It can be seen that the correlations between C_D and Nu are relatively obvious, and Nu is primarily affected by C_D. Besides, under the influence of the upstream vortices, Nu of the midstream and downstream bluff bodies exhibits multi-frequency components. Finally, we conclude that $d/D = 0.7$ and 0.8, $U_r > 9$ can benefit and enhance heat transfer efficiency, owing to the higher Nu_A and the bluff bodies showing moderate amplitudes.

CRediT authorship contribution statement

Junlei Wang: Conceptualization, Investigation, Formal analysis, Writing – original draft, Funding acquisition. **Ye Zhang:** Writing – original draft, Software, Data curation, Visualization. **Guobiao Hu:** Formal analysis, Writing – review & editing, Supervision, Funding acquisition. **Wenming Zhang:** Writing – review & editing, Supervision.

Declaration of Competing Interest

The authors declare that they have no known competing financial interests or personal relationships that could have appeared to influence the work reported in this paper.

Data availability

Data will be made available on request.

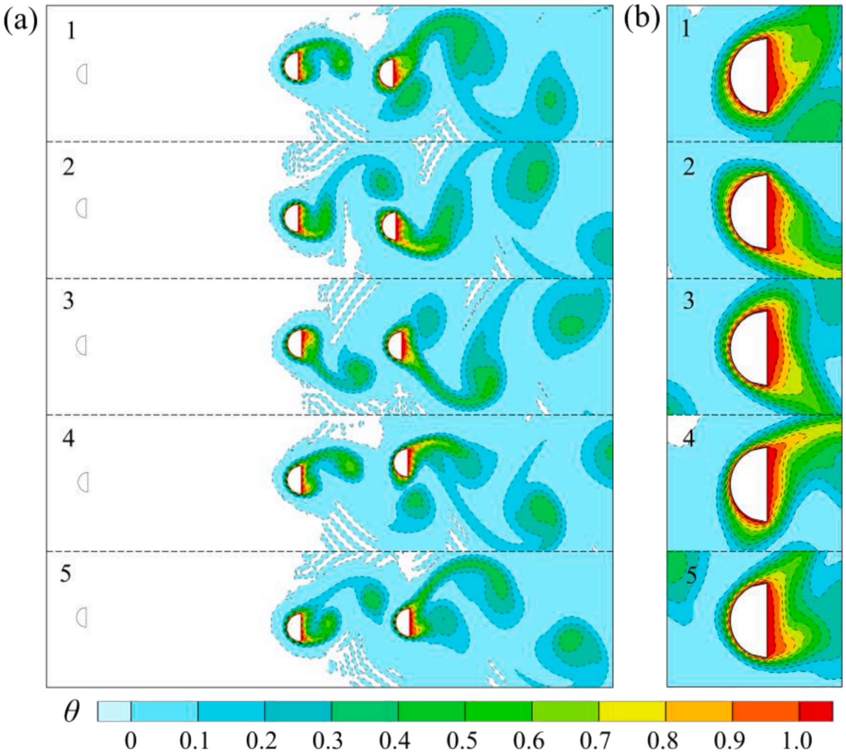

Fig. 31. Corresponding normalized temperature contours at five instants for $d/D = 0.7$, $U_r = 12$: (a) the global normalized temperature contours; (b) the local normalized temperature contours of B3.

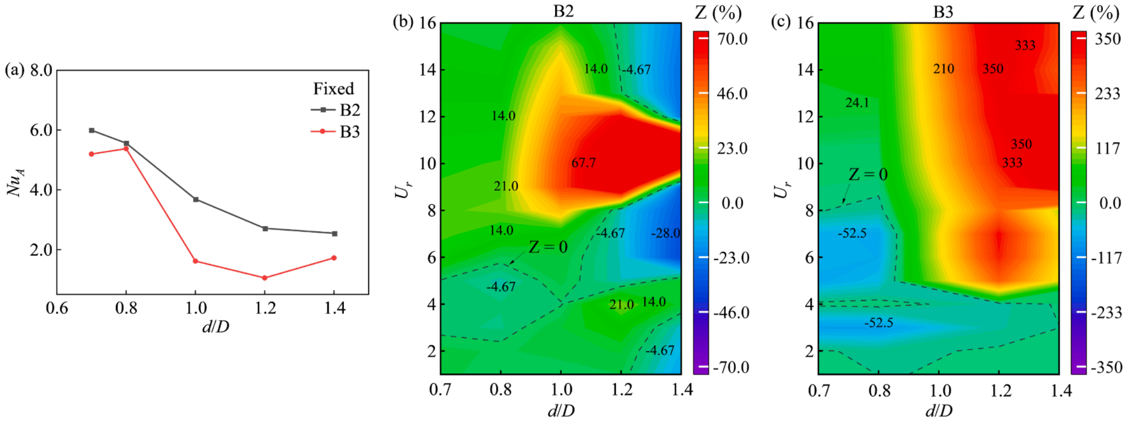

Fig. 32. The Nu_A increase rate Z of B2 and B3: (a) Nu_A changes with d/D in the stationary state; (b) the Nu_{A2} increase rate of B2; (c) the Nu_{A3} increase rate of B3.

Acknowledgments

This work was supported by the National Natural Science Foundation of China (Grant No.: 51977196, 52277227, 52305135), Natural Science Foundation of Excellent Youth of Henan Province (Grant No.: 222300420076), Program for Science & Technology Innovation Talents in Universities of Henan Province (Grant No.: 23HASTIT010), Science and Technology Research & Development Joint Foundation of Henan Province- Young Scientists (Grant No.: 225200810099), National Center for International Research of Subsea Engineering Technology and Equipment, No.: 3132023366, State Key Laboratory of Structural Analysis for Industrial Equipment (GZ21114), and Soyotec Technologies Co., Ltd. (Beijing) on XFlow Software.

References

Ali, U., Islam, M., Janajreh, I., Fatt, Y., Alam, M.M., 2021. Flow-induced vibrations of single and multiple heated circular cylinders: a review. Energies 14 (24), 8496.

Ambreen, T., Kim, M.H., 2018. Flow and heat transfer characteristics over a square cylinder with corner modifications. Int. J. Heat Mass Transf. 117, 50–57.

Ahn, H.T., Kallinderis, Y., 2006. Strongly coupled flow/structure interactions with a geometrically conservative ALE scheme on general hybrid meshes. J. Comput. Phys. 219 (2), 671–696.

Barati, E., Biabani, M., Zarkak, M.R., 2022. Numerical investigation on vortex-induced vibration energy harvesting of a heated circular cylinder with various cross-sections. Int. Commun. Heat Mass Transfer 132, 105888.

Barrero-Gil, A., Serruys, S., Velazquez, A., 2022. Influence of cross-section shape on energy harvesting from transverse flow-induced vibrations of bluff bodies. J. Fluid Mech. 950, A25.

Borazjani, I., Sotiropoulos, F., 2009. Vortex-induced vibrations of two cylinders in tandem arrangement in the proximity-wake interference region. J. Fluid Mech. 621, 321–364.

Cheng, L., Luan, T., Du, W., Xu, M., 2009. Heat transfer enhancement by flow-induced vibration in heat exchangers. Int. J. Heat Mass Transf. 52 (3–4), 1053–1057.

Chen, W.L., Ji, C.N., Williams, J., Xu, D., Yang, L.H., Cui, Y.T., 2018. Vortex-induced vibrations of three tandem cylinders in laminar cross-flow: vibration response and galloping mechanism. J. Fluids Struct. 78, 215–238.

Churchill, S.W., Bernstein, M., 1977. A correlating equation for forced convection from gases and liquids to a circular cylinder in crossflow. Asme Trans. J. Heat Transfer 99 (2), 300–306.

Dai, S.S., Tang, D., Younis, B.A., 2022. Extended wall-adapting local eddy-viscosity model for the large-eddy simulations of multiscale flows. Phys. Fluids 34 (5), 055117.

Darbhamulla, N.B., Bhardwaj, R., 2021. Flow-induced vibrations of circular cylinder in tandem arrangement with D-section cylinder at low Reynolds number. Phys. Fluids 33 (5), 053606.

Dhiman, A.K., Chhabra, R.P., Eswaran, V., 2005. Flow and heat transfer across a confined square cylinder in the steady flow regime: effect of Peclet number. Int. J. Heat Mass Transf. 48 (21–22), 4598–4614.

Ding, L., Zou, Q.F., Zhang, L., Wang, H.B., 2018. Research on flow-induced vibration and energy harvesting of three circular cylinders with roughness strips in tandem. Energies 11 (11), 2977.

Ding, L., Han, Y.X., Yang, Z.M., Zhang, L., He, H.Y., 2022. Influence of upstream cylinder on flow-induced vibration and heat transfer of downstream cylinder. Int. J. Thermal Sci. 176, 107519.

Doerksen, G., Ziade, P., Korobenko, A., Johansen, C., 2022. A numerical investigation of recirculation in axisymmetric confined jets. Chem. Eng. Sci. 254, 117603.

Duan, D.R., Ge, P.Q., Bi, W.B., Ji, J.D., 2017. Numerical investigation on the heat transfer enhancement mechanism of planar elastic tube bundle by flow-induced vibration. Int. J. Thermal Sci. 112, 450–459.

Go, J.S., 2003. Design of a microfin array heat sink using flow-induced vibration to enhance the heat transfer in the laminar flow regime. Sensors Actuators a-Phys. 105 (2), 201–210.

Goyder, H.G.D., 2002. Flow-induced vibration in heat exchangers. Chem. Eng. Res. Design 80 (A3), 226–232.

Hamdan, M.N., Jubran, B.A., Shabaneh, N.H., Abusamak, M., 1996. Comparison of various basic wavelets for the analysis of flow-induced vibration of a cylinder in cross flow. J. Fluids Struct. 10 (6), 633–651.

Huang, C.C., Hsieh, J.S., Chen, P.C., Lee, C.H., 2008. Flow analysis and flow-induced vibration evaluation for low-pressure feed-water heater of a nuclear power plant. Int. J. Pressure Vessels Piping 85 (9), 616–619.

Izadpanah, E., Amini, Y., Ashouri, A., 2018. A comprehensive investigation of vortex induced vibration effects on the heat transfer from a circular cylinder. Int. J. Thermal Sci. 125, 405–418.

Kareem, A., Kijewski, T., 2002. Time-frequency analysis of wind effects on structures. J. WIND ENG. INDUST. AERODYN. 90 (12–15), 1435–1452.

Khan, H.H., Islam, D., Fatt, Y.Y., Janajreh, I., Alam, M., 2022. Flow-induced vibration on two tandem cylinders of different diameters and spacing ratios. Ocean Eng. 258, 111747.

KOIDE, M., TOMIDA, S., TAKAHASHI, T., BARANYI, L., 2002. SHIRAKASHI, and Masataka, influence of cross-sectional configuration on the synchronization of Karman vortex shedding with the cylinder oscillation. JSME int. j. Ser. B, Fluids thermal eng. 45 (2), 249–258.

Kruger, T., Kusumaatmaja, H., Kuzmin, A., Shardt, O., Silva, G., Viggen, E.M., 2017. The Lattice Boltzmann Method. Springer, Switzerland.

Kumar, A., Dhiman, A., Baranyi, L., 2016. Fluid flow and heat transfer around a confined semi-circular cylinder: onset of vortex shedding and effects of Reynolds and Prandtl numbers. Int. J. Heat Mass Transf. 102, 417–425.

Kumar, V., Garg, H., Sharma, G., Bhardwaj, R., 2020. Harnessing flow-induced vibration of a D-section cylinder for convective heat transfer augmentation in laminar channel flow. Phys. Fluids 32 (8), 083603.

Mahendra, A., Kumar, R.S., 2023. Heat exchanger with semi-circular tubes and mountings for effective heat transfer. Numer. Heat Transfer, Part A: Appl. 1–24.

Mahír, N., Altaç, Z., 2008. Numerical investigation of convective heat transfer in unsteady flow past two cylinders in tandem arrangements. Int. J. Heat Fluid Flow 29 (5), 1309–1318.

Nada, S.A., El-Batsh, H., Moawed, M., 2006. Heat transfer and fluid flow around semi-circular tube in cross flow at different orientations. Heat Mass Transf. 43 (11), 1157–1169.

Païdoussis, M.P., Price, S.J., Langre, E.D., 2011. Fluid-Structure Interactions: Cross-Flow-Induced Instabilities, 50. AIAA Journal.

Parthasarathy, N., Dhiman, A., Sarkar, S., 2017. Flow and heat transfer over a row of multiple semi-circular cylinders: selection of optimum number of cylinders and effects of gap ratios. Eur. Phys. J. Plus 132 (12), 532.

Peng, L.H., Gu, X.B., Yang, H.B., Zheng, D.P., Wang, P.Z., Cui, H.Z., 2022. Ultra-high evaporation rate 3D evaporator with vertical sheets based on full use of convection flow. J. Clean. Prod. 345, 131172.

Pettigrew, M.J., Taylor, C.E., 2003a. Vibration analysis of shell-and-tube heat exchangers: an overview - part 1: flow, damping, fluidelastic instability. J. Fluids Struct. 18 (5), 469–483.

Pettigrew, M.J., Taylor, C.E., 2003b. Vibration analysis of shell-and-tube heat exchangers: an overview - part 2: vibration response, fretting-wear, guidelines. J. Fluids Struct. 18 (5), 485–500.

Prasanth, T.K., Mittal, S., 2007. Vortex-induced vibrations of a circular cylinder at low Reynolds numbers. J. Fluid Mech. 594, 463–491.

Prasanth, T.K., Mittal, S., 2009. Vortex-induced vibration of two circular cylinders at low Reynolds number. J. Fluids Struct. 25 (4), 731–741.

Qi, H., Li, X.L., Yu, C.P., 2022. A modified wall-adapting local eddy-viscosity model for large-eddy simulation of compressible wall-bounded flow. Phys. Fluids 34 (11), 116114.

Rajamuni, M.M., Thompson, M.C., Hourigan, K., 2020. Vortex dynamics and vibration modes of a tethered sphere. J. Fluid Mech. 885, A10.

Sareen, A., Zhao, J., Jacono, D.L., Sheridan, J., Hourigan, K., Thompson, M.C., 2018. Vortex-induced vibration of a rotating sphere. J. Fluid Mech. 837, 258–292.

Shi, Y., Zhao, T.S., Guo, Z.L., 2004. Thermal lattice Bhatnagar-Gross-Krook model for flows with viscous heat dissipation in the incompressible limit. Phys. Rev. E Stat. Nonlin. Soft Matter Phys. 70 (6), 066310. Pt 2): p.

Verma, M., De, A., 2022. Thermal cooling enhancements in a heated channel using flow-induced motion. J. Therm. Sci. Eng. Appl. 14 (8), 081003.

Wang, C., Tang, H., Duan, F., Yu, S.C.M., 2016. Control of wakes and vortex-induced vibrations of a single circular cylinder using synthetic jets. J. Fluids Struct. 60, 160–179.

Wang, J.L., Geng, L.F., Ding, L., Zhu, H.J., Yurchenko, D., 2020a. The state-of-the-art review on energy harvesting from flow-induced vibrations. Appl. Energy 267, 114902.

Wang, J.L., Zhao, W., Su, Z., Zhang, G.J., Li, P., Yurchenko, D., 2020b. Enhancing vortex-induced vibrations of a cylinder with rod attachments for hydrokinetic power generation. Mech. Syst. Signal Process 145, 106912.

Wambsganss, M.W. *Heat-exchanger tube vibration: a technical problem in the application and development of heat-recovery systems*. 1981. United States.

Xu, W.H., Ji, C.N., Sun, H., Ding, W.J., et al., 2019. Flow-induced vibration of two elastically mounted tandem cylinders in cross-flow at subcritical Reynolds numbers. Ocean Eng. 173, 375–387.

Yuan, P., Schaefer, L., 2006. Equations of state in a lattice Boltzmann model. Phys. Fluids 18 (4), 042101.

Zafar, F., Alam, M.M., 2018. A low Reynolds number flow and heat transfer topology of a cylinder in a wake. Phys. Fluids 30 (8), 083603.

Zafar, F., Alam, M.M., 2019. Flow structure around and heat transfer from cylinders modified from square to circular. Phys. Fluids 31 (8), 083604.

Zhang, H.X., Wu, X.P., Pan, Y.J., Azam, A., Zhang, Z.T., 2021. A novel vibration energy harvester based on eccentric semicircular rotor for self-powered applications in wildlife monitoring. Energy Convers. Manage. 247, 114674.

Zhu, H.J., Wang, K.N., 2019. Wake adjustment and vortex-induced vibration of a circular cylinder with a C-shaped plate at a low Reynolds number of 100. Phys. Fluids 31 (10), 103602.

Zhu, H.J., Liu, W.L., 2020. Flow control and vibration response of a circular cylinder attached with a wavy plate. Ocean Eng. 212, 107537.

Zhu, H.J., Li, G.M., Wang, J.L., 2020a. Flow-induced vibration of a circular cylinder with splitter plates placed upstream and downstream individually and simultaneously. Appl. Ocean Res. 97, 102084.

Zhu, H.J., Tang, T., Wang, J.L., 2020b. Modification of wake flow and air-bubble-vortex interference in the flow control of a circular cylinder with a pair of air jets: effect of injection velocity. Ocean Eng. 214, 107766.

Zhu, H.J., Zhong, J.W., Zhou, T.M., 2021. Wake structure characteristics of three tandem circular cylinders at a low Reynolds number of 160. Phys. Fluids 33 (4), 044113.

Zhang, C.M., Zhang, X.T., Zhao, F., Gerada, D., et al., 2022. Improvements on permanent magnet synchronous motor by integrating heat pipes into windings for solar unmanned aerial vehicle. Green Energy Intell. Transp. 1 (1), 100011.

Zhu, H.J., Hu, J., Alam, M.M., Ji, C.N., Zhou, T.M., 2022a. Hydrodynamic characteristics and wake evolution of a submarine pipe with the presence of gas leakage at a low Reynolds number of 160. Phys. Fluids 34 (8), 083609.

Zhu, H., Zhong, J., Liu, B., 2022b. Fluid–thermal–structure interaction of three heated circular cylinders in tandem at a low Reynolds number of 150. Phys. Fluids 34 (8), 083605.